AGU
ADVANCING EARTH AND SPACE SCIENCES

JGR Planets

Key Points:

- The South Apollo basin exhibits three periods of mare basaltic volcanism (*EmSAp1*, *EmSAp2* and *EmSAp3*) separated by one billion years
- Chang'e 6 landed on the ~2.81 Ga old mare unit (*EmSAp2*)
- The returned samples consist of materials with multiple sources, including 70% of local basaltic material and 30% of distant ejecta

Supporting Information:

Supporting Information may be found in the online version of this article.

Correspondence to:

L. Xiao,
longxiao@cug.edu.cn

Geological Background of the Chang'e 6 Landing Site and the Provenance of Returned Samples

Antong Gao[1] [ID], Long Xiao[1,2] [ID], Lukas Wueller[3] [ID], Wajiha Iqbal[3] [ID], Siyuan Zhao[1], Jiang Wang[1], Carolyn H. van der Bogert[3] [ID], Yuqi Qian[4] [ID], Yong Pang[5], and Harald Hiesinger[3] [ID]

[1]Planetary Science Institute, School of Earth Sciences, China University of Geosciences, Wuhan, China, [2]State Key Laboratory of Lunar and Planetary Sciences, Space Science Institute, Macau University of Science and Technology, Macao, China, [3]Institut für Planetologie, Universität Münster, Münster, Germany, [4]Department of Earth Sciences & Laboratory for Space Research & NWU-HKU Joint Center of Earth and Planetary Sciences, The University of Hong Kong, Hong Kong, China, [5]Beijing Spacecrafts, China Academy of Space Technology, Beijing, China

Abstract China's Chang'e-6 (CE-6) is the first mission in human history to return samples from the far side of the Moon. CE-6 landed in the mare plains of the southern Apollo basin (153.98°W, 41.63°S) within the South Pole-Aitken (SPA) basin on 2 June 2024 and returned 1,935.3 g of samples on 25 June 2024. The unique geological history of the Apollo basin offers an opportunity to address several important scientific questions in lunar science. To provide geological context for the analysis of the returned samples, we described the geology of the area surrounding the CE-6 landing site in detail. We interpreted that the region exhibits three periods of mare basaltic volcanism (*EmSAp1*, *EmSAp2* and *EmSAp3*) separated by one billion years. CE-6 landed on the *EmSAp2* unit, with a model age of ~2.8 Ga. Several post-mare impacts occurring outside this region also contributed foreign materials to CE-6 landing site. We anticipate that the returned samples are dominated by local *EmSAp*2 materials, and may also include younger high-Ti basalt from the *EmSAp3* unit, older low-Ti basalt from the *EmSAp1* unit, ejecta from younger craters such as Chaffee S and O'Day, and ejecta from craters outside the SPA basin such as Vavilov, Crookes, and Das. The estimated total feldspathic exotic ejecta in the regolith of CE-6 sample zone is 30%. Our study indicates that the regolith in the CE-6 sampling area is rich in scientific value for understanding lunar volcanism and impact history and offers the possibility of further calibrating the lunar cratering chronology.

Plain Language Summary For a long time, South Pole-Aitken (SPA) basin on the Moon has been regarded as a key region in lunar exploration. In 2024, China's Chang'e-6 probe obtained the world's first lunar far-side sample from the Apollo Basin within the SPA basin. Based on remote sensing data, we analyzed the geological characteristics surrounding the CE-6 landing site and reconstructed the geological history of this area. Our results indicate that the Chang'e-6 landed on a mare unit with an age of approximately 2.81 Ga, younger than Apollo landing sites but older than the Chang'e-5 landing site. The returned samples have multiple sources of materials, dominated by the ~2.8 Ga aged basalts and may also consist of 30% feldspathic materials from multiple impact craters. Based on this, we propose that Chang 'e-6 samples have the potential to solve several key scientific questions.

1. Introduction

The Apollo peak-ring basin, with a diameter of 492 km (Neumann et al., 2015), is the largest impact basin within the South Pole-Aitken (SPA) basin (Baker et al., 2011). The Apollo basin formed in the northeastern portion of the SPA basin, partly within the SPA transient crater and modification zone (Potter et al., 2018). The Apollo basin may have formed 3.98 billion years ago (Ivanov et al., 2018) and potentially excavated material from ~30 km depth (Potter et al., 2018). Subsequent impacts modified the Apollo basin and redistributed crater materials, such as impact melt deposits from the Apollo basin floor. Additionally, multiple mare basalt units have been identified within the Apollo basin, with previous studies proposing various hypotheses on the volcanic history of this region (Haruyama et al., 2009; Pasckert et al., 2018; Qian et al., 2024; Zeng et al., 2023).

Unraveling the history and evolution of the Apollo basin also requires understanding of the underlying SPA basin, the largest (2,400 × 2,050 km) and oldest known impact basin on the Moon (Garrick-Bethell & Zuber, 2009; Hiesinger & Head, 2004), which provides a window into the lunar interior. For instance, modeling of SPA-scale impact events (Melosh et al., 2017) predicts that deep crustal and shallow mantle materials were excavated (Potter

et al., 2012). As such, SPA-derived materials have a distinctive composition with higher FeO and Th abundances compared to the feldspathic highlands, but lower than the Procellarum KREEP Terrane (Jolliff et al., 2000). Pyroxenes are the most abundant mafic minerals in the SPA basin. With increasing distance from the center of the SPA basin, the composition of pyroxene changes gradually, showing a trend from calcium-rich iron clinopyroxenes (CPX) to magnesium-rich orthopyroxenes (OPX) (Moriarty & Pieters, 2016, 2018; Pieters et al., 2001). To potentially sample materials derived from great depths without drilling, it is likely advantageous to collect samples from the interior of the SPA basin (Jolliff et al., 2021).

The SPA basin is also a record of lunar early impact events and farside volcanic activity, as it contains multiple Nectarian and Pre-Nectarian impact basins (Orgel et al., 2018; Wilhelms et al., 1987) for which sample ages are not yet available to calibrate the lunar cratering chronology (van der Bogert & Hiesinger, 2020). Additionally, several isolated mare basalt deposits are located on the floor of the SPA basin (Haruyama et al., 2009; Pasckert et al., 2018), illustrating significant differences in the volume and distribution of mare between the nearside and farside. To better calibrate the early impact history and to explain the evolution of lunar volcanism and the origin of the lunar nearside–farside dichotomy, sampling materials from the SPA basin is essential and has been listed as a top lunar mission priority (Smith et al., 2006).

To achieve these key scientific objectives, China launched the CE-6 mission on 3 May 2024, and returned 1,935.3 g of samples from the mare plain in the southern Apollo basin (153.98°W, 41.63°S) on 25 June 2024 (Liu et al., 2024). This is a new milestone in the history of human lunar exploration, with scientific mysteries hidden in the samples awaiting discovery by scientists (Yang et al., 2024). Several groups have reported the geological context of the sampling area. However, work to date shows differences between their interpreted geologic units and geological history (Chen et al., 2022; Fortezzo et al., 2020; Ivanov et al., 2018; Orgel et al., 2024; Qian et al., 2024), and lacks essential detailed geological mapping with absolute model ages (AMAs) for the key geological units. To measure precise AMAs for the sampling and adjacent units, we first defined geological units and their contacts based on high-resolution imagery, topographic, and spectral data. Then we defined count areas for crater-size-frequency-distribution (CSFD) measurements to obtain AMAs for the major units in the CE-6 landing zone. Based on this work, we analyze and discuss the potential scientific value of the lunar regolith returned by the CE-6 mission.

2. Method

2.1. Data Sets

In this study, we analyzed the regional geomorphologic characteristics using the Lunar Reconnaissance Orbiter Camera (LROC) Wide Angle Camera (WAC) mosaic (100 m/pixel (Robinson et al., 2010);). Additionally, we utilized the Kaguya Terrain Camera (TC) orthographic mosaic (10 m/pixel) (Haruyama et al., 2008) and high-resolution mosaics (2.2 m/pixel) generated from LROC Narrow Angle Camera (NAC) data (Robinson et al., 2010) to analyze local context. Our mosaic consists of individual high-incidence angle NAC images (ground azimuth direction 270°) with illumination angles ranging between 55° and 85°. The SLDEM2015 (SELENE and LRO DEM 2015) digital elevation model or DEM (Barker et al., 2016) and the Kaguya TC digital terrain model (DTM) were used for topographic analysis. The SLDEM has a resolution of 59 m/pixel, whereas the Kaguya TC DTM has a resolution of 10 m/pixel (Haruyama et al., 2014).

Kaguya Multiband Imager (MI) data (Ohtake et al., 2008) were used to gain insight into the spectral characteristics and composition of the research area. The absolute abundances of TiO_2 and FeO were calculated from MI data (Otake et al., 2012). We also produced false-color composite images with Kaguya MI data, using a method based on processing Clementine multispectral data. The color assignment for false-color images is 750 nm/415 nm as red, 750 nm/950 nm as green, and 415 nm/750 nm as blue (Eliason et al., 1999; Pieters et al., 1994). Compared with the Clementine near-infrared camera, the Kaguya MI has a similar wavelength band but a higher spatial resolution. The false-color composite images highlight differences in surface maturity and composition between different geological units, serving as a crucial basis for determining geological unit boundaries. This method was also used by previous researchers for the geological mapping of the Chang'e-5 landing zone (Qian et al., 2018).

Mineralogical characteristics of the study area were investigated using mosaics generated by Lemelin et al. (2016), which include the abundances of plagioclase, orthopyroxene, clinopyroxene, and olivine, as well as

derived optical maturity (OMAT) mosaics. These maps were created through quantitative mineralogical analyses using reflectance data from the Kaguya MI and radiative transfer modeling (Lemelin et al., 2015, 2016, 2019).

The local maps of these datasets were used in the Orthographic projection.

2.2. Geologic Mapping

The mapping area covers the CE-6 landing zone and adjacent terrain (148°W–158° W, 40°S–45°S) with a digital map scale of 1:250,000. The chronostratigraphic system of this geological map is adapted from Wilhelms et al. (1987), and the symbology used follows the guidelines of the Federal Geographic Data Committee (2006).

The identification of contacts between geological units is based on the topography, albedo and spectral differences. The non-mare units were defined by their higher elevation, higher albedo, and red color in the Kaguya MI false-color images. The mare units were identified as dark plains located in low elevation areas, which show blue, purple, or yellow in the Kaguya MI false-color images. We defined different kinds of contacts between the units: certain, spectral, and inferred. Certain contacts were used for well-defined unit boundaries, while inferred contacts denote less well-defined and transitional contacts. The spectral contacts are defined by differences in albedo and spectral characteristics, such as variations in TiO_2 or FeO abundances and OMAT.

2.3. CSFD Measurements

We used CSFD measurements to determine AMAs for the major geologic units in our map. We selected geologically homogeneous count areas, avoiding secondary crater clusters and chains (Hiesinger et al., 2011, 2023; McEwen & Bierhaus, 2006; Neukum, 1983). Next, we measured the craters with a diameter larger than 10 m within these count areas on our generated LRO NAC mosaic with 2.2 m/pixel resolution. The craters were measured using Crater Tools in ArcMap (Kneissl et al., 2011) and later plotted in Craterstats II (Michael & Neukum, 2010). The AMAs were calculated by the production function (PF) and chronology function (CF) of Neukum (1983). To make comparisons, we also adopted the chronology system updated by Yue et al. (2022) in the measurements. This research performed a randomness analysis to assess and adjust for the possible influence of secondary craters (Michael et al., 2012).

2.4. Identifying Regolith Components

To examine the regolith components in the CE-6 sampling zone, we counted the number of bright rock fragments on the surface using Mathematica 13.2. The first step involved manually identifying the rock fragments in the on-site image taken by the monitor camera on the CE-6 lander. Then, we processed the image using the Filling Transform and Binarize functions to separate the rock fragments from the background. Finally, the component measurement function was used to statistically analyze the pixel proportion of bright rock fragments.

3. Geological Map

The CE-6 lander touched down on a mare basalt plain in the southern part of the Apollo basin (Figures 1b and 2a), which is at a similar latitude to the landing site of CE-4 (Figure 1a). Our mapping zone spans the outer ring of the Apollo basin (the yellow rectangle in Figure 1b). This area can be broadly categorized into three main geological units: mare basalts, non-mare materials, and crater materials (Figure 3). Here, we describe the subdivision of each category into the individual mapped units we defined.

3.1. Mare Basalts

Mare basalt covers the central part of the study area, forming a flat lava plain covering an area of approximately $8.3 \times 10^3 \, km^2$. The area was calculated in a Mollweide projection map. The average elevation of the basalt plain is −5,166 m. Besides the dark albedo and flat topography of the mare units seen in optical datasets, the compositions of the basalts are markedly different from the surrounding basin and impact materials, as seen in spectral data. Indeed, these spectral data can also aid in the separation of different mare basalt units. Thus, we used the Kaguya MI color ratio product that we generated (Figure 4a) to identify the spectral contacts of the different mare units in the mapping area. In general, the mare units exhibit much lower plagioclase abundances (Figure 4b) and much higher FeO and TiO_2 abundances (Figures 4c and 4d) than the surrounding terrain. The different mare units are
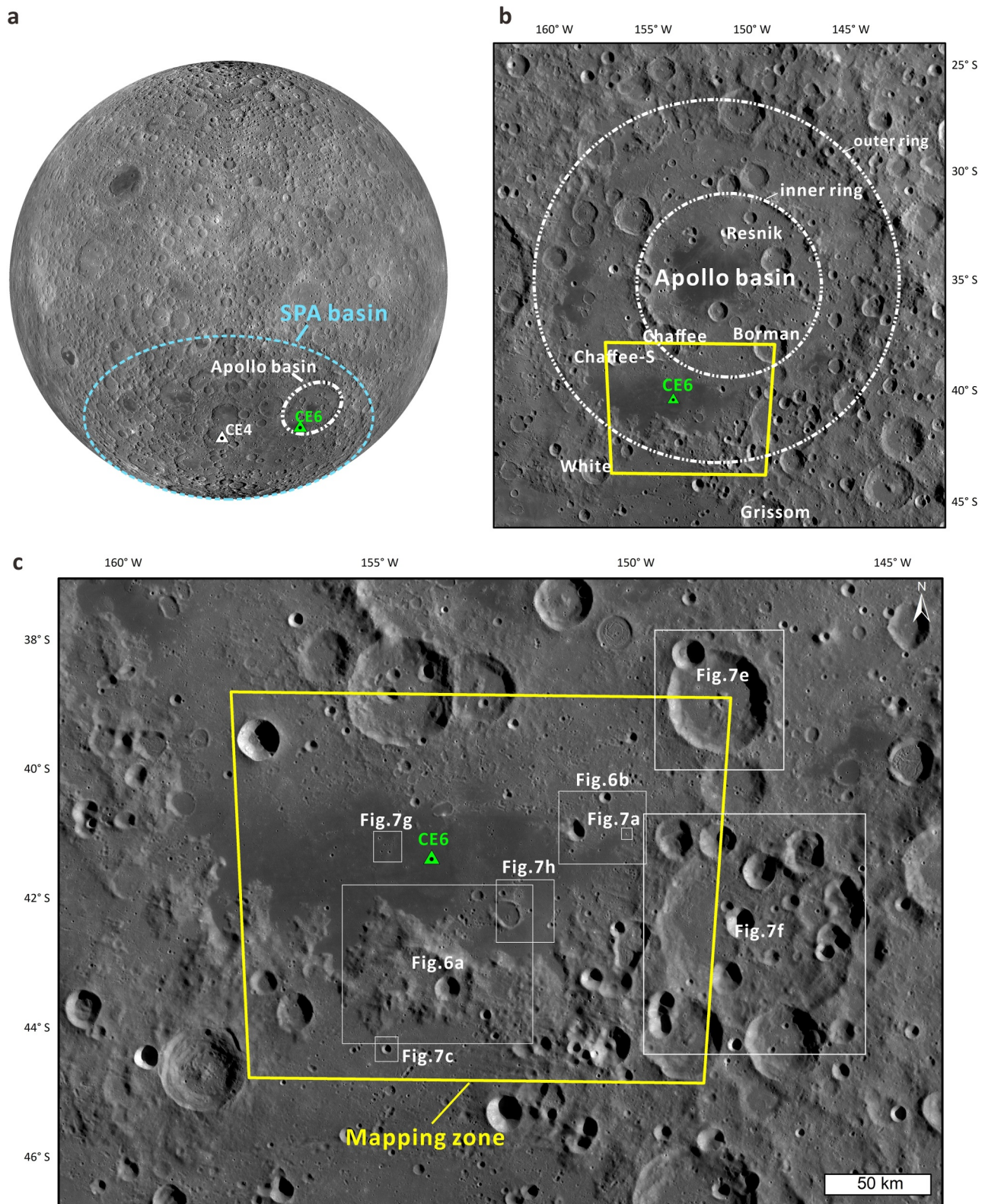
Figure 1. Regional context of the CE-6 landing site: (a) the location of Apollo basin within the South Pole-Aitken basin, and (b) Apollo basin as shown on the LRO wide-angle camera (WAC) global mosaic (100 m/pixel), (c) Mapping zone and surrounding area in LRO wide-angle camera (WAC) global mosaic (100 m/pixel). These images were projected by the Orthographic projection. In Figure 1a, the longitude of center is 180°W and the latitude of center is 0°S. In Figures 1b and 1c, the longitude of center is 154°W and the latitude of center is 43°S.
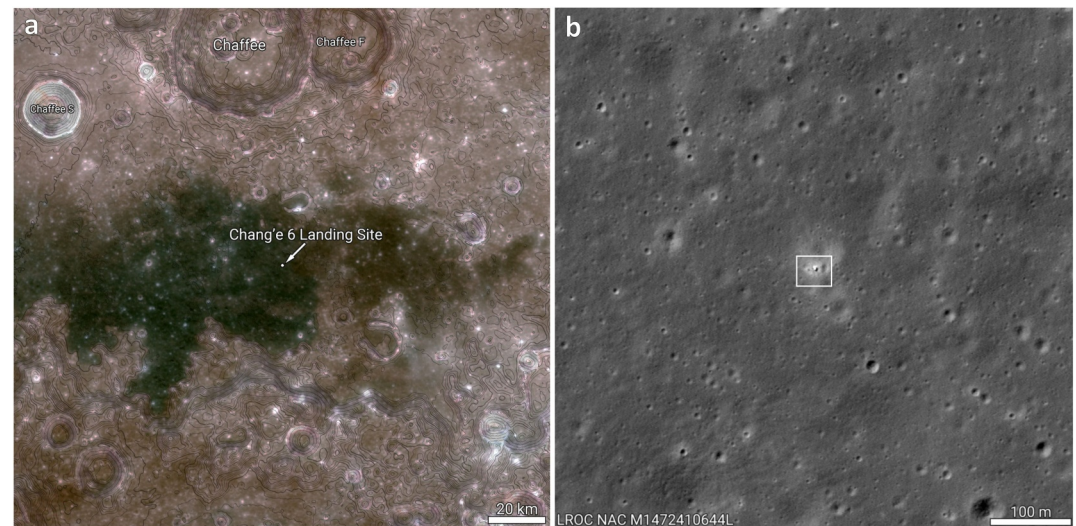
Figure 2. Overview of the CE-6 Landing Site, (a) LRO WAC Empirical Color Mosaic of the southern Apollo basin area, the contour lines mark 100-m elevation intervals, (b) narrow angle camera image M1472410644 L capturing CE-6 (within white box) on the lunar surface (https://www.lroc.asu.edu/images/1374). The resolution of this image is 0.94 m/pixel.

subdivided as described in the next paragraph. Due to the sharp spectral boundaries visible, we used Kaguya MI band ratio false-color images to identify the spectral contact of the mare units in the study area (Figure 4a).

Eastern part of Eratosthenian Mare 1 in Southern Apollo basin (EmSAp1-E): The *EmSAp1* mare unit is located in the southern Apollo basin and is divided into two subunits: *EmSAp1*-E and *EmSAp1*-W. The *EmSAp1* is overlain by *EmSAp2* unit in the central portion of the mare-covered area (Figure 3). In the eastern *EmSAp1*-E unit, the
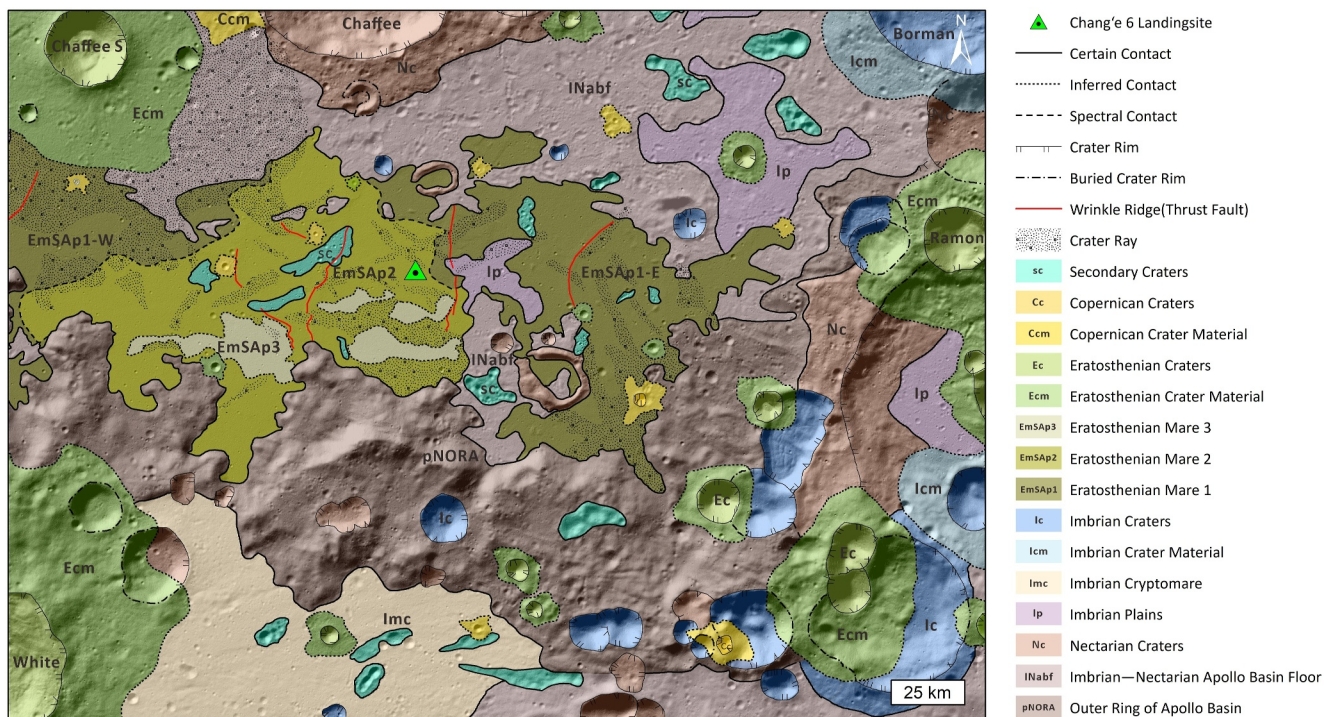
Figure 3. Geological map of the CE-6 landing zone and surrounding areas. This map shows 16 different units, including mare units (EmSAp1, EmSAp2 and EmSAp3), non-mare units (pNORA, INabf, Ip, Imc) and crater units (crater rays, sc, Cc, Ccm, Ec, Ecm. Ic, Icm, Nc). A SLDEM2015 hillshade product was used as a basemap. The figure was projected by the Orthographic projection (longitude of center: 154°W, latitude of center: 43°S).
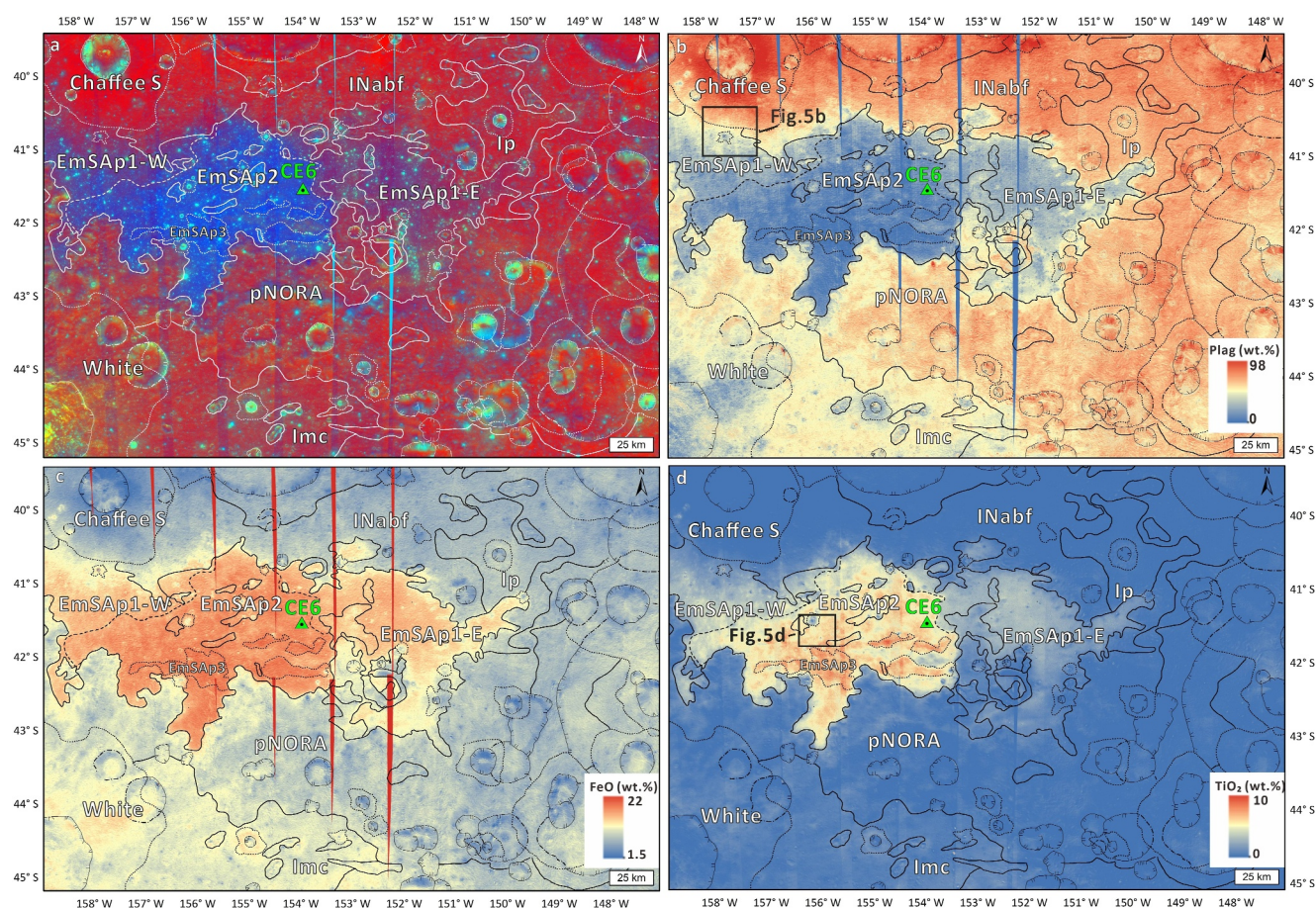
Figure 4. The mapping area with unit contacts shown on the Kaguya multiband imager (MI) (Ohtake et al., 2008) (a) false color composite image, red is non-mare material, purple is low titanium mare material and blue is high titanium mare material, (b) plagioclase abundance map, (c) FeO abundance map, and (d) TiO_2 abundance map produced by Kaguya MI data. These figures were projected by the Orthographic projection (longitude of center: 154°W, latitude of center: 43°S).

surface appears red to purple in the Kaguya MI false-color images (Figure 4a), with an average TiO_2 content of 3.66 wt.%, FeO content of 17.3 wt.%, and plagioclase content of 38.5 wt.% (Figure 4). According to the classification of mare basalt proposed by Fagan and Neal (2016), the *EmSAp1*-E is a low-Ti basalt unit. In *EmSAp1*-E, the overlying ejecta blankets from young impact craters exhibit signatures rich in plagioclase. Of these, craters with diameters over 1,500 m penetrated the mare basalt layer and excavated the underlying non-mare material. According to the excavation depth equation for impact craters proposed by Melosh (1989) ($D_{exc} \approx 0.084D_r$, where D_{exc} is the excavation depth and D_r is the crater diameter), we estimate that the basalt thickness in *EmSAp1*-E is less than 120 m.

Western part of Eratosthenian Mare 1 in the Southern Apollo basin (EmSAp1-W): EmSAp1-W has similar characteristics to the eastern mare unit *EmSAp1*-E (Figure 3), but is covered by bright, plagioclase-rich materials (>55 wt.%) (Figure 4b) in the ejecta and ray material from the Chaffee S crater. Near the inferred contact with the Chaffee S crater ejecta blanket, we identified a dark-halo impact crater DHC-1 (Figure 5a). The ejecta from this younger crater has a lower plagioclase abundance (~35 wt.%) (Figure 5b) and lower albedo compared to the surrounding area, indicating that the crater excavated dark mare basalt from beneath the bright ejecta. The fresh mare basaltic material excavated by DHC-1 has an average TiO_2 content of 3.4 wt.%, FeO content of 16.44 wt.% and plagioclase content of 35.3% (Table 1). According to the classification method mentioned above (Fagan & Neal, 2016), *EmSAp1*-W is also a low titanium basalt unit, which is similar to *EmSAp1*-E. Based on the superposition of the Chaffee S ejecta material on the mare unit, the *EmSAp1*-W low titanium mare basalt unit formed earlier than Chaffee S.
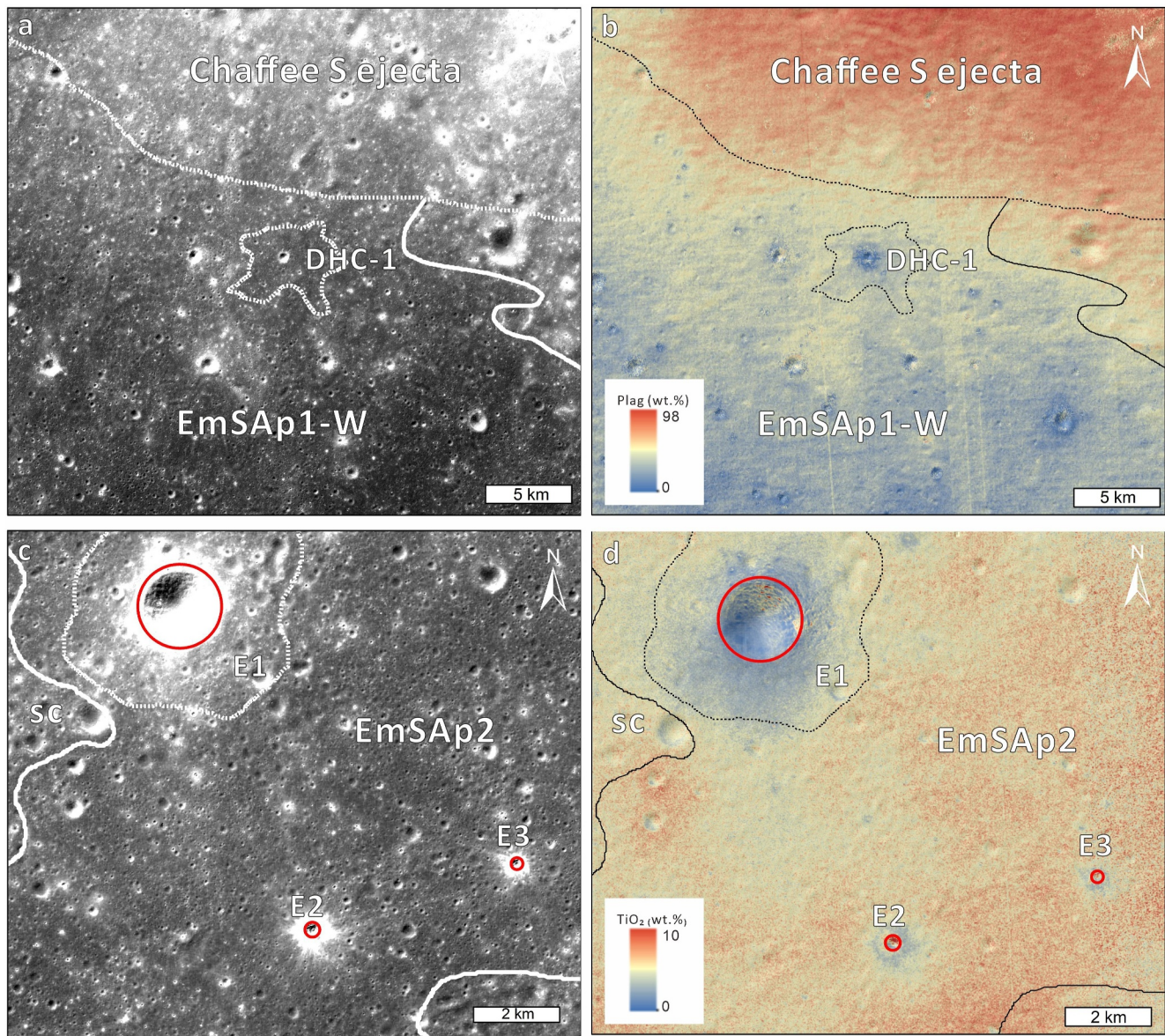
Figure 5. A dark-halo crater near the contact between EmSAp1-W and Chaffee S crater in panel (a) terrain camera orthographic mosaic and (b) multiband imager (MI) plagioclase abundance map. (c) Three craters (red circles) with diameters of 2,068 m (E1), 371 m (E2), and 270 m (E3) in the EmSAp2 unit that penetrated through the high TiO_2 basalt, shown in panel (c) TC orthographic mosaic and (d) MI TiO_2 abundance map. These figures were projected by the Orthographic projection (longitude of center: 154°W, latitude of center: 43°S).

Eratosthenian Mare 2 in Southern Apollo basin (EmSAp2): The *EmSAp2* unit is located in the central part of the basalt plain (Figure 3) and appears bright blue in the Kaguya MI false-color images (Figure 4a). This unit is characterized by medium to high TiO_2 (∼6.2 wt.%) and high FeO (∼18.1 wt.%) contents. According to the classification method mentioned above (Fagan & Neal, 2016), the *EmSAp2* basalt is a high Ti basalt. However, the TiO_2 content in the *EmSAp2* unit is not homogeneous. The surface of the EmSAp2 basalt unit is partly covered by multiple bright impact crater ejecta rays. The mixing of in situ materials and impact ejecta resulted in an increase in albedo and lower TiO_2 and FeO content. Furthermore, young impact craters exhibit low-Ti ejecta covering high-Ti mare basalt. We also identified impact craters within the *EmSAp2* region that penetrated the high-Ti basalt layer and excavated medium to low TiO_2 material (3–4 wt.%) (such as E1 to E3 crater in Figure 5).

Table 1
The Average Compositions of the Mare Units (wt.%)

	FeO	TiO₂	Plag	Cpx	Opx	Ol
EmSAp3	19.6	8.6	31.4	36.1	22.9	11.4
EmSAp2	18,1	6.2	35.4	30.1	23.7	10.7
EmSAp1-E	17.3	3.66	38.5	21.7	32.9	6.9
EmSAp1-W	16.44	3.4	35.3	28	26.3	10

By estimating the depth of excavation, we can infer the thickness of the *EmSAp2* basalt unit. The minimum diameter of craters in the *EmSAp2* unit that exposes low-Ti ejecta is 280 m (Figures 5c and 5d). Depending on the relationship between the crater diameter and excavation depth mentioned above, we estimate the thickness of the *EmSAp2* unit to be around 20 m. In addition, the ejecta blankets of impact craters larger than 1,200 m show characteristics consistent with their excavation of non-mare material (rich in plagioclase). According to the relationship between the crater diameter and excavation depth, the total thickness of mare basalt in the area is approximately 100 m. Thus, *EmSAp2* is interpreted to consist of a thin layer of high-ti basalt (20 m thick) overlying the *EmSAp1* (80 −100 m thick).

EmSAp3: In the central and southern parts of the *EmSAp2* unit, there are several dark patches that still exhibit lower albedo and higher TiO_2 (8.6 wt.%), FeO (19.6 wt.%) content and lower plagioclase abundance (∼31.4 wt.%) compared to the surrounding areas. We mapped these low albedo patches as *EmSAp3* units. This unit may represent smaller-scale, younger basaltic activities. They formed later than the main impact events within the study area (such as Chaffee S), and therefore were not covered by the bright ejecta rays.

3.2. Non-Mare Units

In the geological map shown in Figure 3, the non-mare units are divided into the outer ring structure of the Apollo basin (*pNORA)*, an Imbrian-Nectarian Apollo Basin Floor unit (*INabf* unit), which has a significantly degraded surface and has been heavily modified by subsequent impacts; the Imbrian cryptomare unit (*Imc)*, and the light plains unit (*Ip)*. In the false-color images, the non-mare units appear red, similar to the highland material (Figure 4a). However, compared to the surrounding lunar highlands, which belong to the Feldspathic Highlands Terrane (FHT), the non-mare units in the study area are more enriched in orthopyroxene (∼20 wt.%). We primarily identified the contacts of the non-mare units based on topography and morphology.

Pre-Nectarian Outer Ring of Apollo basin (pNORA): The *pNORA* unit is a remnant rim structure of the Apollo basin (Figure 3), standing 300–1,500 m higher in elevation than the mare plains that fill parts of the basin. *pNORA* features significant terrain undulations, with a smooth surface and heavily degraded impact craters. In the northern part of the study area, *pNORA* is partially infilled by mares (Figures 6c and 6d). In the eastern part of the study area, *pNORA* is truncated by the *INabf* and *Nc* units, while in the southern part, it is partially covered by the *Imc* unit. These geomorphic relationships indicate that the *pNORA* unit is the oldest geological unit in the region.

Imbrian-Nectarian Apollo Basin Floor (INabf): The *INabf* unit represents the post-Apollo basin surface, containing highly degraded and rugged terrain that has not been completely overprinted by subsequent activity (Figure 3). In the study area, *INabf* is mainly identified at the northern edge of the region, with an average elevation of −4,579 m (Figure 6b). Additionally, the *INabf* unit appears as isolated kipukas or island-like land forms within the mare basalt plains (Figures 6c and 6d).

Imbrian plains (Ip): With an average surface elevation of −5,426 m (Figure 6b), the *Ip* unit (Figure 3) is characterized by a flat surface with similar albedo to the *INabf* unit and a high plagioclase abundance (∼70 wt.%; Figure 4b). Superimposed impact craters with diameters up to 1.6 km are abundant. The light plains (*Ip*) are primarily distributed in the topographic lows within the highly degraded Nectarian and pre-Nectarian units (*pNORA* and *INabf*; Figure 6a). Based on their distribution in topographic depressions, composition, and morphology, we interpret the light plains to be ejecta from basin-forming impact events. One candidate is the impact that formed the Orientale basin, which is about 1,500 km away and has been suggested to have formed other light plain deposits on the Moon (Meyer et al., 2020; Qiao et al., 2024)

Imbrian cryptomare (Imc): The *Imc* unit (Figure 3) is situated south of the outer rim domain of the Apollo basin (Figure 6c). In multispectral imagery, the ejecta blankets around the craters on this unit reveal clinopyroxene-rich material (Figure 4c), indicating that a subsurface layer containing mafic minerals such as clinopyroxene is being exposed. Based on our observations, we interpret the *Imc* unit as cryptomare. The excavation depth of craters that penetrated the light surface layer suggests a light plain thickness of up to 160 m covering the underlying mare.

3.3. Impact Craters

Because impact events expose and eject subsurface materials, and ejecta can even be sampled far from the craters, it is critical to understand the impact processes and their timing to enhance the scientific value of returned samples from the Apollo basin by the CE-6 mission. We have classified impact craters within our study area into Nectarian
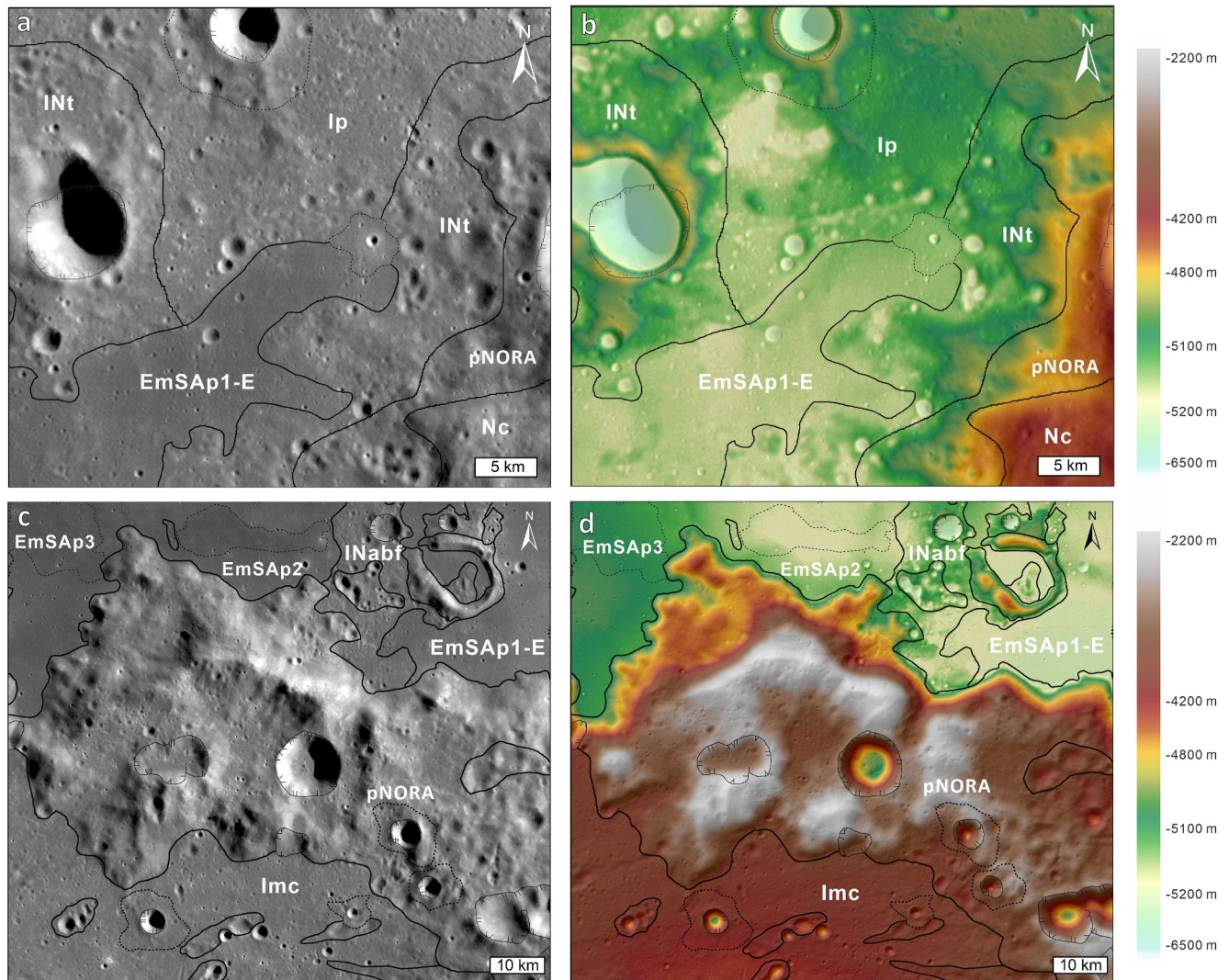
Figure 6. Morphological characteristics and contacts in the northeastern part of the study area shown on a (a) WAC mosaic, and (b) SLDEM2015; and in the central part of the study area shown on a (c) WAC mosaic and (d) SLDEM2015. These figures were projected by the Orthographic projection (longitude of center: 154°W, latitude of center: 43°S).

(*Nc*), Imbrian (*Ic*), Eratosthenian (*Ec*), and Copernican (*Cc*) craters in the geological map shown in Figure 3, based on their morphology, degradation (Fortezzo & Hare, 2013; Head, 1975; Wilhelms et al., 1987), and their optical maturity feature (OMAT). OMAT is a unitless value that represents the degree of space weathering on the surface (Lucey et al., 2000). Following previous research, older craters have lower OMAT values, whereas younger craters have higher OMAT values (Grier et al., 2001).

Nectarian craters (Nc): Nectarian impact craters typically exhibit highly degraded crater walls and are often covered by younger craters and ejecta (Figure 7f). They have low OMAT values (average value of 0.13), and there are no prominent ejecta blanket landforms around these craters. These craters are mainly distributed on the rugged surfaces of the *pNORA* and *INabf* units within the region, while some are covered by mare and light plains materials (such as Chaffee crater and the unnamed crater in Figure 7f).

Imbrian Craters (Ic): Compared to Nectarian craters, Imbrian craters show an intermediate degree of degradation. Typical Imbrian craters in the mapping zone (e.g., Borman crater) have discernible ejecta blankets and flat crater floor. Their topography appears subdued compared with younger craters (Figure 7e). Imbrian craters are widely distributed in geological units outside *EmSAp1* and *EmSAp2*.
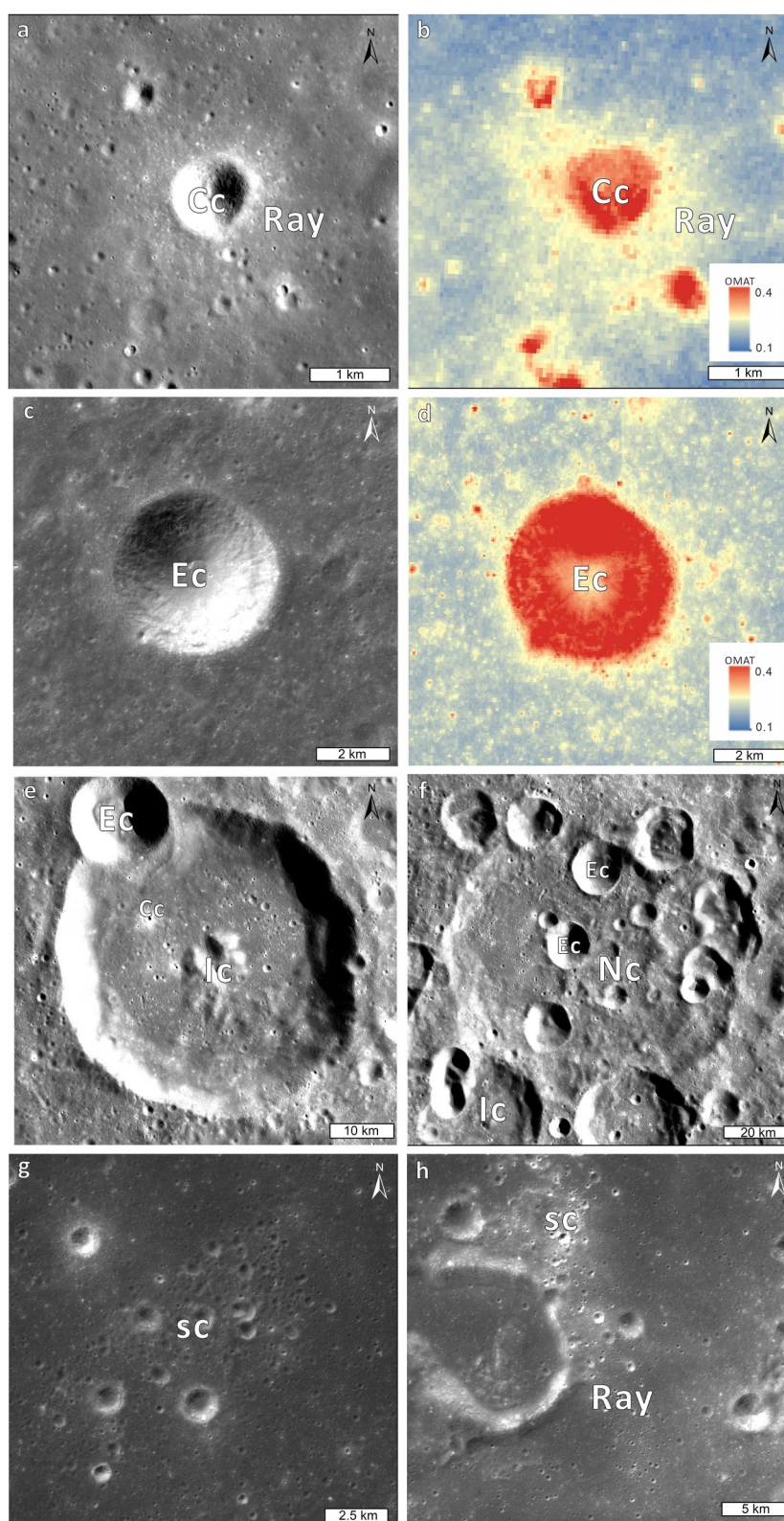
Figure 7. Examples of crater classes mapped in the study area: Copernican crater in panel (a) terrain camera (TC) orthographic mosaic and (b) OMAT; Eratosthenian crater in (c) TC orthographic mosaic and (d) OMAT; (e) Imbrian crater, and (f) Nectarian crater in TC orthographic mosaic; (g)–(h) Secondary crater clusters and crater rays in TC orthographic mosaic. These figures were projected by the Orthographic projection (longitude of center: 154°W, latitude of center: 43°S).

Eratosthenian craters (Ec): Eratosthenian craters have relatively sharp rims and steeper crater walls than Imbrian craters (Figure 7c). Additionally, they have higher OMAT values on the crater rim (with an average value of 0.34, Figure 7d), although the ejecta shows low OMAT values (with an average value of 0.1). Among the named impact craters in the study area, Chaffee S and White craters were classified in our work as Eratosthenian impact craters. Both craters have relatively sharp crater walls, and their ejecta blankets, which show significant compositional differences from the surrounding surfaces, are relatively intact. The ejecta blanket of Chaffee S crater is characterized by low Fe content and significantly higher plagioclase content compared to other geological units. In contrast, the ejecta from White crater is enriched in mafic minerals and has a relatively low plagioclase content (Figures 4b and 4c).

Copernican craters (Cc): Copernican impact craters have sharp rims and steep crater walls. Their ejecta and rays are easily identifiable in visible light images (Figure 7a). The Copernican crater rims have a similar OMAT value compared to that of Eratosthenian craters (with an average value of 0.35). The OMAT value of the Copernican crater ejecta blanket is higher (with an average value of 0.2) than the OMAT value of Eratosthenian craters (Figure 7b).

Secondary Craters (sc): Secondary craters are generally shallower than primary craters, due to their less energetic impacts (lower impact velocity) compared to primary impacts. Secondary craters often appear in clusters or chains and can be identified by their non-circular, irregular shapes, overlaps, and similar levels of degradation (Figures 7g and 7h). Around the CE-6 landing site, a chain of shallow secondary craters points to the Chaffee S crater in the northwest (Figure 2b).

Rays: Rays are identified as discontinuous distal ejecta, distinguished by their reflectance and compositional characteristics that contrast with the undisturbed underlying geologic units (Figure 7h). The presence of rays significantly impacts on the analysis of the potential scientific value of the surface regolith and the selection of count areas for CSFD measurements (Hiesinger et al., 2012). A NW-SE trending ray is located near the CE-6 landing site, so the samples from CE-6 might contain this material. To emphasize the importance of distal ejecta in this study, we classified ejecta rays as separate geologic units in our geologic map (Figure 3).

3.4. Structures

Several wrinkle ridges have been identified within the mare plains. These ridges predominantly trend NE-SW, with lengths ranging from 5 to 28 km, heights from 10 to 100 m, and slopes between 1° and 6°. Golombek and McGill (1983) suggest that the formation of wrinkle ridges is related to the subsidence process of impact basins. Some of the wrinkle ridges cut through the spectral contact between the *EmSAp2* and *EmSAp1*-E units. The relationships between these ridges and other units indicate that these structures are younger than the *EmSAp2* unit in the region (Figure 3).

4. Age Determinations

We estimated the surface age of the region around the landing site of CE-6 (in the *EmSAp2* unit). Additionally, we determined the AMAs of other major plains-forming units defined in our geologic map for the CE-6 landing zone (Figure 3; *EmSAp1*, *EmSAp3*, and *Imc*).

We also present a CSFD-based AMA for White crater to determine its formation sequence relative to the three main plain units. Considering the significant heterogeneity and limited distribution of each unit in the study area, we carefully delineated the counting areas to avoid secondary craters, rays, topographical variations, and compositional inconsistencies (Figure 8). For crater counting, we used a high-resolution NAC mosaic with a resolution of 2.2 m/pixel. The randomness analysis shows that in most areas, potential secondary crater clusters occur for crater diameters smaller than 75 m. Therefore, we excluded this diameter range for fitting the $N(1)$ values.

4.1. Crater Size-Frequency Distribution (CSFD) Measurement of CE-6 Landing Site (*EmSAp2*)

Determining the surface age of the surrounding area of the CE-6 sampling site can provide a direct reference for future sample analysis. The CE-6 sampling site is located within the *EmSAp2* basalt unit (Figure 8b). Based on the geological mapping conducted in this study, a 27 km² counting area was selected around this point, avoiding the bright ejecta identified on the geological map we produced (Figures 8a and 8b). Fitting the CSFD for crater
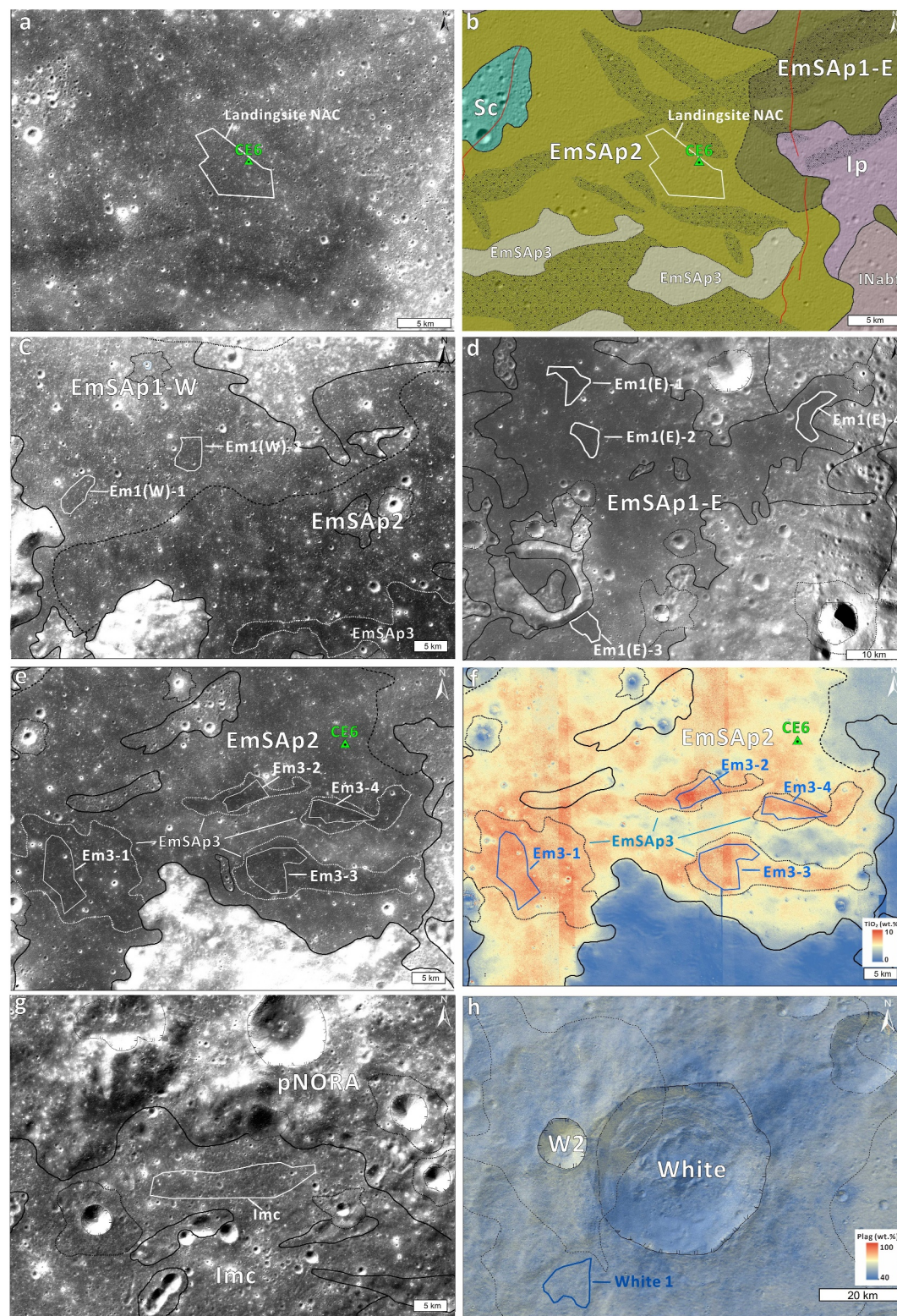
Figure 8. Count areas for crater size-frequency distribution measurements. (a)–(b) CE-6 Landing site (EmSAp2 unit), (c) EmSAp1-W, (d) EmSAp1-E, (e)–(f) EmSAp3, (g) Imc and (h) White crater ejecta. The base map for panels (a), (c), (d), (e) and (g) is the Kaguya terrain camera orthographic mosaic; for panel (b) is the geology map in this study, for panel (f) is the multiband imager (MI) TiO$_2$ abundance map and for panel (h) is the MI plagioclase abundance map. These figures were projected by the Orthographic projection (longitude of center: 154°W, latitude of center: 43°S).

Table 2
N(1)Values of Counting Areas in LRO Narrow Angle Camera Images

| Area name	Area [km^2]	No. of craters fit	Fit range [m]	PF/CF: Neukum (1983)			PF: Neukum et al. (2001) CF: Yue et al. (2022)		
				N$_{cum}$ (D ≧ 1 km)[km^{-2}]	AMA [Ga]	AMA error [Ga]	N$_{cum}$ (D ≧ 1 km)[km^{-2}]	AMA [Ga]	AMA error [Ga]
CE-6 landingsite (EmSAp2)									
Landingsite	27.5	59.5	150–450	2.37×10^{-3}	2.81	+0.26\−0.33	2.27×10^{-3}	2.91	+0.21\−0.32
Imc									
Imc-1	95	27.2	490–1,400	2.31×10^{-3}	3.84	+0.027\−0.033	2.31×10^{-3}	3.84	+0.027\−0.033
EmSAp1-E									
Em1 (E) −1	23	54.6	150–500	2.30×10^{-3}	3.14	+0.14\−0.28	2.30×10^{-3}	3.18	+0.11\−0.22
Em1 (E) −2	18.6	56	150–400	3.39×10^{-3}	3.34	+0.07\−0.12	3.25×10^{-3}	3.34	+0.063\−0.099
Em1 (E) −3	17	25.5	170–600	3.09×10^{-3}	3.26	+0.12\−0.32	2.97×10^{-3}	3.28	+0.11\−0.25
Em1 (E) −4	26.1	45	170–500	2.80×10^{-3}	3.15	+0.14\−0.30	2.68×10^{-3}	3.19	+0.12\−0.24
SUM *EmSAp1*-E	84.9	211.9	150–700	2.88×10^{-3}	3.19	+0.07\−0.10	2.77×10^{-3}	3.22	+0.056\−0.078
EmSAp1-W									
Em1 (W) −1	14.8	42	150–500	2.89×10^{-3}	3.19	+0.13\−0.29	2.77×10^{-3}	3.22	+0.11\−0.22
Em1 (W) −2	16.3	39.7	150–500	2.83×10^{-3}	3.16	+0.14\−0.32	2.72×10^{-3}	3.20	+0.12\−0.25
SUM *EmSAp1*-W	31.1	82.7	150–600	2.83×10^{-3}	3.16	+0.11\−0.2	2.71×10^{-3}	3.20	+0.089\−0.15
White crater									
White-1	80.2	82.2	160–360	2.41×10^{-3}	2.85	+0.2\−0.26	2.31×10^{-3}	2.95	+0.16\−0.24
		5	800–1,300	2.74×10^{-3}	3.87	+0.059\−0.1	2.75×10^{-3}	3.87	+0.059\−0.1
EmSAp3									
Em3-1	40.4	67.1	140–600	1.59×10^{-3}	1.89	+0.22\−0.22	1.53×10^{-3}	1.99	+0.24\−0.24
Em3-2	14.6	41.3	120–300	1.88×10^{-3}	2.24	+0.32\−0.32	1.81×10^{-3}	2.36	+0.33\−0.34
Em3-3	37.7	107.7	120–700	1.65×10^{-3}	1.97	+0.18\−0.18	1.59×10^{-3}	2.08	+0.19\−0.19
Em3-4	18.6	74.7	110–250	1.72×10^{-3}	2.05	+0.22\−0.22	1.66×10^{-3}	2.25	+0.21\−0.21
SUM *EmAp3*	111.3	317.7	120–700	1.63×10^{-3}	1.94	+0.1\−0.1	1.57×10^{-3}	2.05	+0.12\−0.12

diameters from 150 to 450 m, we obtained an $N(1)$ value of 2.37×10^{-3} km^{-2} for the area around the landing site by cumulative fitting, corresponding to an AMA of $2.81 + 0.26\backslash-0.33$ Ga using the PF and CF of Neukum (1983). If using the chronology system proposed by Yue et al. (2022), we got an AMA of $2.91 + 0.21\backslash-0.32$ Ga for the sampling site (Table 2).

4.2. Crater Size-Frequency Distribution (CSFD) Measurements to Other Major Plains-Forming Units

Imc: For the *Imc* unit in the southern part of the study area, we selected a flat count area of 95 km^2 (Figure 8g). Fitting the CSFD for diameters between 490 and 1,400 m, we obtained an $N(1)$ value of 2.31×10^{-3} km^{-2}, corresponding to an AMA of $3.84 + 0.027\backslash-0.033$ Ga (Figure 9, Table 2) using the chronology system of Neukum (1983). If using the chronology system proposed by Yue et al. (2022), we got an AMA of $3.84 + 0.027$ \−0.033 Ga for Imc unit.

EmSAp1-E: Using our new geological map as a reference, we selected four count areas with a total area of 84.9 km^2 (Figure 8d) with similar high FeO content and homogeneous low albedo, while avoiding the rays and secondary craters. Using the cumulative plot and fitting the CSFD for diameters between 150 and 700 m, we obtained an $N(1)$ value of 2.88×10^{-3} km^{-2} for the *EmSAp1*-E unit, corresponding to an AMA of $3.19 + 0.07$ \−0.1 Ga using the chronology system of Neukum (1983). If using the chronology system proposed by Yue
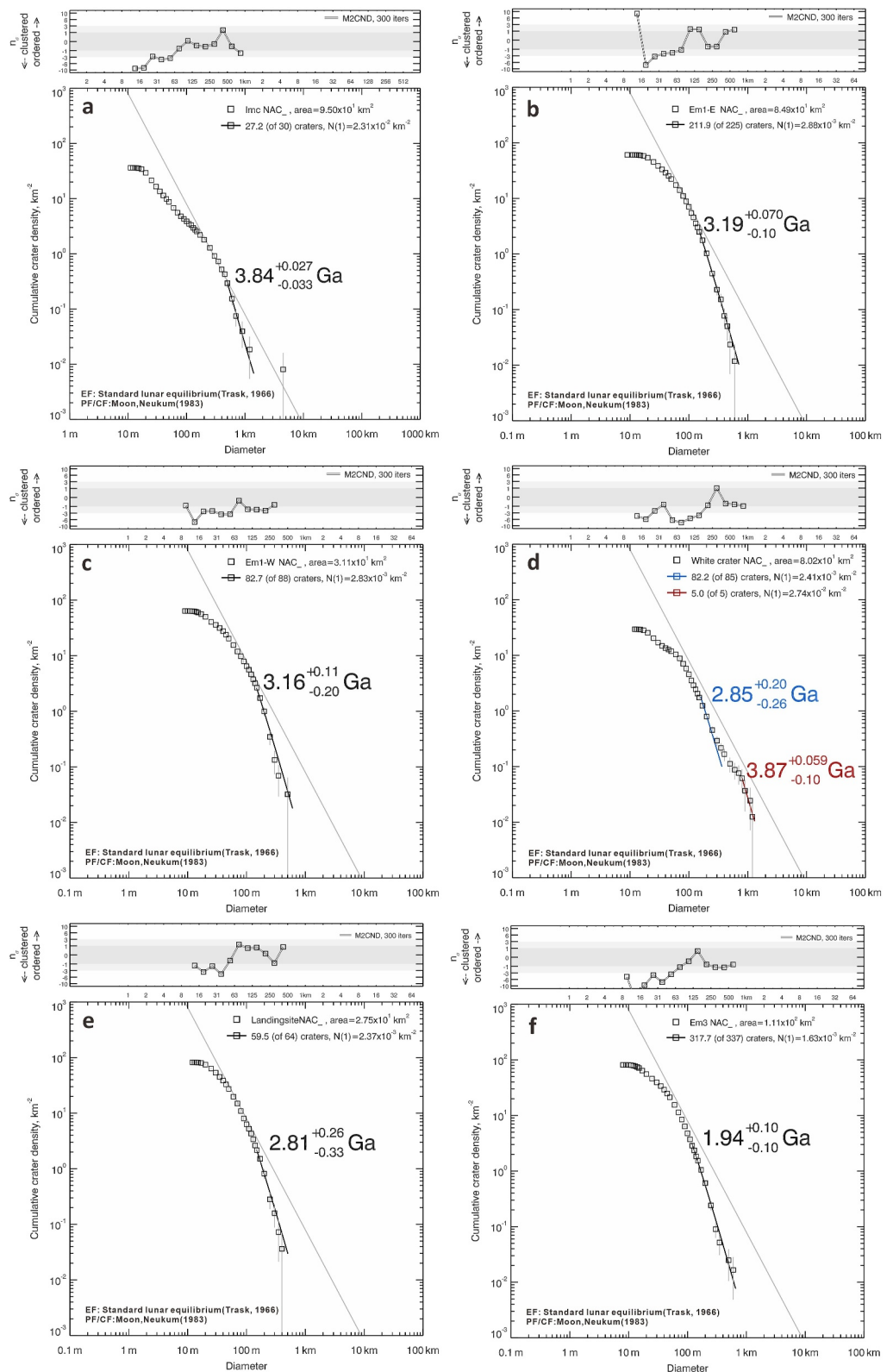
Figure 9. CSFDs and fitted AMAs for the (a) Imc, (b) EmSAp1-E, (c) EmSAp1-W, (d) White crater, (e) EmSAp2 and (f) EmSAp3. See Table 2 for details.

et al. (2022), we got an AMA of 3.22 + 0.056\−0.078 Ga for *EmSAp1*-E unit. Individual CSFD measurements for the four regions also yielded similar age results (Table 2).

EmSAp1-W: Although the *EmSAp1*-W unit has been significantly influenced by the Chaffee S crater ejecta, we managed to define two count areas containing homogeneous low albedo, totaling 31.1 km^2 (Figure 8c). The CSFDs for Em1(W)-1 and Em1(W)-2 yielded similar ages (3.19 Ga and 3.16 Ga). After merging these two measurements, we fitted the CSFD for diameters between 150 and 600 m and obtained an *N*(1) value of 2.83 × 10⁻³ km^{-2} using the chronology system of Neukum (1983), corresponding to an AMA of 3.16 + 0.11 \−0.2 Ga, which is within the same error range as the *EmSAp1*-E unit.

EmSAp3: For the potentially young basalt *EmSAp3*, we selected four count areas (totaling 111.3 km^2) within the low albedo patches (Figures 8e and 8f). Fitting the CSFD for diameters between 120 and 700 m, we obtained an *N*(1) value of 1.63 × 10⁻³ km^{-2} by cumulative fitting, corresponding to an AMA of 1.94 ± 0.1 Ga using the chronology system of Neukum (1983). If using the chronology system proposed by Yue et al. (2022), we got an AMA of 2.05 ± 0.12 Ga for the *EmSAp3* unit. Individual measurements for each region also yielded similar results (Table 2).

White crater: We outlined a flat count area on the ejecta blanket near the southern rim of the White crater (Figure 8h). The CSFDs from this area indicate two surface ages (Figure 9). The surface age of the larger crater bins (800–1,300 m) is estimated to be 3.87 + 0.059\−0.1 Ga, which is very similar to the AMA of the nearby *Imc* unit. Conversely, the surface age of the smaller crater bins (160–360 m) is estimated to be 2.85 + 0.2\−0.26 Ga (Table 2) using the chronology system of Neukum (1983), which we interpret to represent the formation age of White crater. If using the chronology system proposed by Yue et al. (2022), we also got a similar AMA of 2.95 + 0.16\−0.24 Ga. According to this result, the White crater may have formed in the Eratosthenian period.

5. Discussion

5.1. Mapping and CSFD Results

Haruyama et al. (2009) summarized all mare basalts in the study region into their *Apollo-S* mare units. In geologic mapping of the Apollo basin (Ivanov et al., 2018; Orgel et al., 2024) and the 1:5M scale global geologic map of the Moon (Fortezzo et al., 2020), the basaltic plains in the study area are also assigned to Imbrian volcanism. Pasckert et al. (2018) suggested that the mare plain in the study area should be divided into two units, *Ap4* and *Ap5*. The *Ap4* unit roughly corresponds to the *EmSAp2* and *EmSAp1*-W units in this study, with an AMA of 3.31 Ga (Pasckert et al., 2018). The *Ap5* mare unit of Pasckert et al. (2018) corresponds to the *EmSAp1*-E units in this study, with an AMA of 3.45 Ga. Recently, Qian et al. (2024) divided the mare plain into *Southern Mare Unit 1* (corresponding to the *Ap4* unit) and *Southern Mare Unit 2* (corresponding to the *Ap5* unit), with AMAs of 3.07 + 0.07\−0.08 Ga and 3.34 + 0.04\−0.06 Ga.

Haruyama et al. (2009), Ivanov et al. (2018), Pasckert et al. (2018), Orgel et al. (2024), and Qian et al. (2024) suggest that all mare units in the southern Apollo basin were formed before 3 Ga. However, our CSFD measurements indicate at least two distinct periods of volcanic activity in the southern Apollo basin (Figure 3). At 3.2 Ga, the first period of basaltic activity formed the low-titanium basalt unit infilling the southern Apollo basin. From 2.8 Ga, high-titanium basalt spread from the central part of the previous basalt unit with smaller eruptions. Zeng et al. (2023) also indicated that there was a younger period of volcanic activity in Region F (*EmSAp2* unit in this study). Additionally, Y. Wang et al. (2024) and Yue et al. (2024) report similar CSFD results. Our calculated AMA for the *EmSAp2* (2.81 Ga) unit is older than the other determined ages in the region: 2.4 Ga (Zeng et al., 2023) and 2.49 Ga (Y. Wang et al., 2024) or 2.5 Ga (Yue et al., 2024) for Region F (Table 3). The differences may be due to previous works selecting a non-uniform counting area. According to the description in Chapter 3, this research has identified a new basalt unit *EmSAp3* inside the *EmSAp2* unit (Region F in previous study), which represents possible young mare basalt activity in the mapping zone. Therefore, Zeng et al. (2023) probably obtained a mixed age that included two periods of volcanic activity in the mapping zone.

For the potentially young mare basalt unit *EmSAp3*, we obtained similar results across the four counting areas. This suggests that volcanic activity in the southern Apollo basin was more persistent than previously thought (Y. Wang et al., 2024; Yue et al., 2024; Zeng et al., 2023). Additionally, we determined that the high-Ti region in the mare basalt plain had the longest duration of activity in the mapping area. This hypothesis aligns with the microwave thermophysical features measured by the Chang'E Lunar Microwave Sounder (CELMS) onboard the

Table 3
Comparison of the AMAs of Geologic Units Around CE-6 Landing Site With Previous Studies

|	*Imc* [Ga]	*EmSAp1*-E [Ga]	*EmSAp1*-W [Ga]	*EmSAp2* [Ga]
AMAs in this research	3.84	3.19	3.11	2.81
PF/CF: Neukum (1983)	(+0.027\−0.033)	(+0.07\−0.10)	(+0.11\-0,2)	(+0.26\−0.33)
Haruyama et al. (2009)	-		2.44	
PF/CF: Haruyama et al. (2009)				
Whitten and Head (2015) PF: Neukum et al. (2001) CF: Neukum et al. (2001)	3.88 (+0.06\−0.1)	-	-	-
Pasckert et al. (2018) PF: Neukum et al. (2001) CF: Neukum et al. (2001)	-	3.45 (+0.04\−0.05)	3.31 (±0.02)	
Zeng et al. (2023) PF: Neukum et al. (2001) CF: Yue et al. (2022)	3.86 (+0.036\−0.048)	3.43 (+0.041\−0.061)	-	2.4 (±0.11)
Qian et al. (2024) PF: Neukum et al. (2001) CF: Yue et al. (2022)	-	3.34 (+0.04\−0.06)	3.07 (+0.07\−0.08)	
Y. Wang et al. (2024) PF: Neukum et al. (2001) CF: Yue et al. (2022)	-	3.27 (+0.036\−0.045)	2.68 (+0.093\−0.095)	2.49 (+0.072\−0.073)

CE2 satellite. The central region of the mare plain has the highest normalized brightness temperature (nTB) in the study zone, implying that in the late stage of mare volcanism, the volcanic activity only occurred in that region (Meng et al., 2019).

For the non-mare units in the study area, similar geological units to the *Ip* unit in this study are referred to as the Cayley Formation (Wilhelms & McCauley, 1971) or light plains (Meyer et al., 2018, 2020). The extent of *Ip* unit in our study shows differences in the west side of the mapping zone compared to Ivanov et al. (2018). As we conducted higher resolution geological mapping and considered the multi-spectral features, we relabeled the light plain around the Chaffee S crater as the *EmSAp1*-W mare unit. Except for that part, the extent of the light plain unit is similar to the extent mapped by Ivanov et al. (2018) and Orgel et al. (2024). Meyer et al. (2020) suggested that the formation of light plains (*Ip*) units in the study zone may be related to the formation of the Orientale basin.

The cryptomare units in the southern part of the study area were similarly identified and mapped by Ivanov et al. (2018), and recent analyses of the global distribution of cryptomare support our demarcation of the *Imc* unit (Ma et al., 2023; Whitten & Head, 2015). The CSFD results for the mapped *Imc* unit are align with the Zeng et al. (2023) results in their region B (Table 3). Recent studies on the volcanic history of the SPA region (Moriarty et al., 2022; X. Wang et al., 2024) and global distribution analysis of cryptomare (Ma et al., 2023; Whitten & Head, 2015) support the *Imc* unit as a potential cryptomare unit.

The Chaffee-S and White craters are two ejecta sources examined by previous studies (Jia et al., 2024; Zeng et al., 2023). Due to its small diameter and thin ejecta blanket, we could not find suitable counting areas on the Chaffee-S crater ejecta blanket for determining its age. Nevertheless, its morphological features, including a sharp crater rim with a higher OMAT value (∼0.32) compared to the Imbrian craters (such as Borman crater) and intact ejecta with a lower OMAT value (∼0.13) compared with Copernican craters (such as W2 crater), suggest that the Chaffee S crater is older than 0.8 Ga. Considering the morphology relationships discussed in Section 3.1, we believe there is sufficient evidence to support that the formation of the Chaffee-S crater occurred after the *EmSAp2* unit was emplaced (2.81 Ga) and before the formation of the *EmSAp3* unit(1.94 Ga). Therefore, we consider Chaffee-S to be an Eratosthenian crater, contrary to previous geological maps (Chen et al., 2022; Fortezzo et al., 2020; Ivanov et al., 2018; Orgel et al., 2024). According to our CSFD results, the White crater formed at about 2.85 Ga, which matches the observed morphological features and relationships. It is also similar to the classification in existing 1:2.5 M (Chen et al., 2022) and 1:5M global geology maps (Fortezzo et al., 2020).
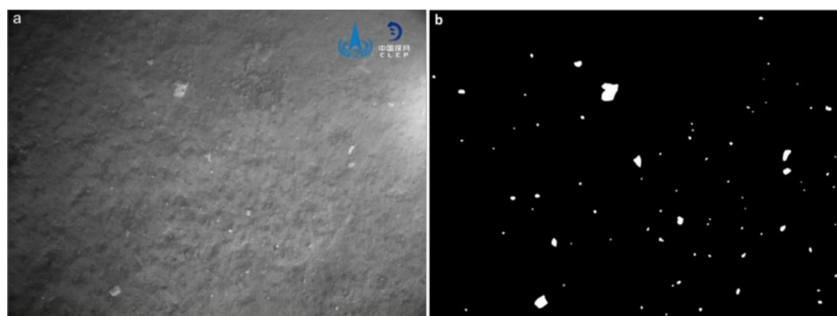
Figure 10. Characteristics of rock fragments at the CE-6 landing site. (a) In situ image of the drilling point, taken by the monitor camera of CE-6 lander (image from CNSA/CLEP). (b) Image extraction results of the bright rock fragments produced by filling transform and binarize functions in Mathematica 13.2.

The AMA of White crater (2.85 Ga) is pretty close to the *EmSAp2* unit (2.81 Ga). Whether there is a correlation between the two results is still up for discussion.

5.2. Provenance of the Regolith in CE-6 Landing Site

According to the geological mapping in our study, the CE-6 landing site is located in the northeastern part of the *EmSAp2* basalt unit, near the boundary between the *EmSAp2* and *EmSAp1*-E units (Figure 3). Therefore, the regolith at the CE-6 landing site may contain local *EmSAp2* high-Ti basalt as well as the *EmSAp1* low-Ti basalt. Our map also shows that the CE-6 landing site is close to a NW-SE trending ray (Figures 8a and 8b, and Figure S1 in Supporting Information S1). In the NAC images, a series of highly degraded impact craters, possibly secondary crater clusters, can also be identified in the area surrounding the CE-6 landing site (Figure 2b). This indicates that the CE-6 landing site may be significantly influenced by ejecta from distant impact craters (e.g., Chaffee S, O'Day, Vavilov). For craters with diameters from 2 to 45 km, we estimated their potential ejecta thicknesses at the landing site using the model of Sharpton (2014). For craters with diameters between 45 and 300 km, we used the model of Housen et al. (1983).

5.2.1. Chaffee S Crater

According to the analysis of remote sensing data, the Chaffee S crater material is within the field of noritic anorthosite, which contains 78 wt% plagioclase and 20 wt.% orthopyroxene. The CE-6 landing site is located on a faint northwest-southeast trending bright ray, which points to the Chaffee S crater. In the images of the drilling point taken by the CE-6 monitor camera, fine-grained bright rock fragments are present on the surface, comprising approximately 1% of the lunar regolith content (Figure 10). We speculate that the Chaffee S crater has delivered ejecta to the regolith of the CE-6 landing site in the form of these bright rock fragments. Based on the ejecta deposition model of Sharpton (2014), we estimate the thickness of the Chaffee S ejecta in this area to be approximately 16 cm (Table 4). According to the regolith gardening model proposed by Costello et al. (2018), if the surface age of CE-6 landing site is 2.8 Ga, top 95 cm regolith would be mixed up. We can assume that the ejecta layer from Chaffee S was mixed into the top 95 cm regolith, and its proportion is about 17%.

5.2.2. White Crater

To define the stratigraphic sequence, we compared the White crater ejecta with the CE-6 sample. Recent remote sensing data analysis indicates that the White crater material exhibits noritic lithology within the field of gabbroic norite. The primary mafic mineral of the White crater ejecta is likely orthopyroxene (Jia et al., 2024). The White crater would transport 46 cm ejecta to CE-6 landing site and have a significant influence on the regolith component. However, the latest mineralogy analysis of the CE-6 surface regolith sample shows that the CE-6 soil contains 19.7%augite, 10%pigeonite, and only 3.6% orthopyroxene (Li et al., 2024). Therefore, we propose that White crater would not be a major provenance of CE-6 surface regolith. It is also possible to find more noritic fragments in the drill sample.

Table 4
Ejecta Thicknesses Calculated for Distant Craters at the CE-6 Landing Site

Crater	Diameter	Lon	Lat	Ejecta thickness(cm)
Craters within the SPA basin				
Chaffee S	20.5	157.48°W	39.77°S	16.4
R1	12.7	151.12°W	33.96°S	0.2
W2	12.5	160.22°W	44.59°S	0.5
O'Day	71.0	157.3°E	30.4°S	0.3
Craters out of the SPA Basin				
Das	36.5	137.01°W	26.47°S	0.5
Crookes	50.00	165.09°W	10.41°S	1.3
Vavilov	96.65	138.83°W	0.86°S	7.2
Jackson	71.46	163.32°W	22.04°N	0.8
Guthnik	36.3	94.08°W	47.78°S	0.3
Sharonov	79.6	173.08°E	12.26°N	1.4

5.2.3. Copernican Craters Within the SPA Basin

According to the results mentioned above, White crater is older than the *EmSAp2* basalt unit where the CE-6 landing site is located. Other southwest-northeast trending bright rays may originate from the younger Copernican-aged W2 crater to the west of White crater, named in Jia et al. (2024), and an unnamed crater to the west of Resnik crater in the central Apollo basin, provisionally named R1 (Figure S1 in Supporting Information S1). The combined ejecta thicknesses from these two craters at the landing site are estimated to be about 0.7 cm (Table 4). A young crater near Chaffee crater (labeled C1 in Figure S1 in Supporting Information S1) may be the source of one south-north trending ray in *EmSAp2*, but its ejecta thickness at the CE-6 landing point is less than 0.1 cm. Additionally, the distant O'Day crater (Figure S2 in Supporting Information S1) may also have transported about 0.3 cm of ejecta to the landing site (Table 4); the proportion of Copernican craters within the SPA basin in the top 95 cm of regolith would be 1.1%.

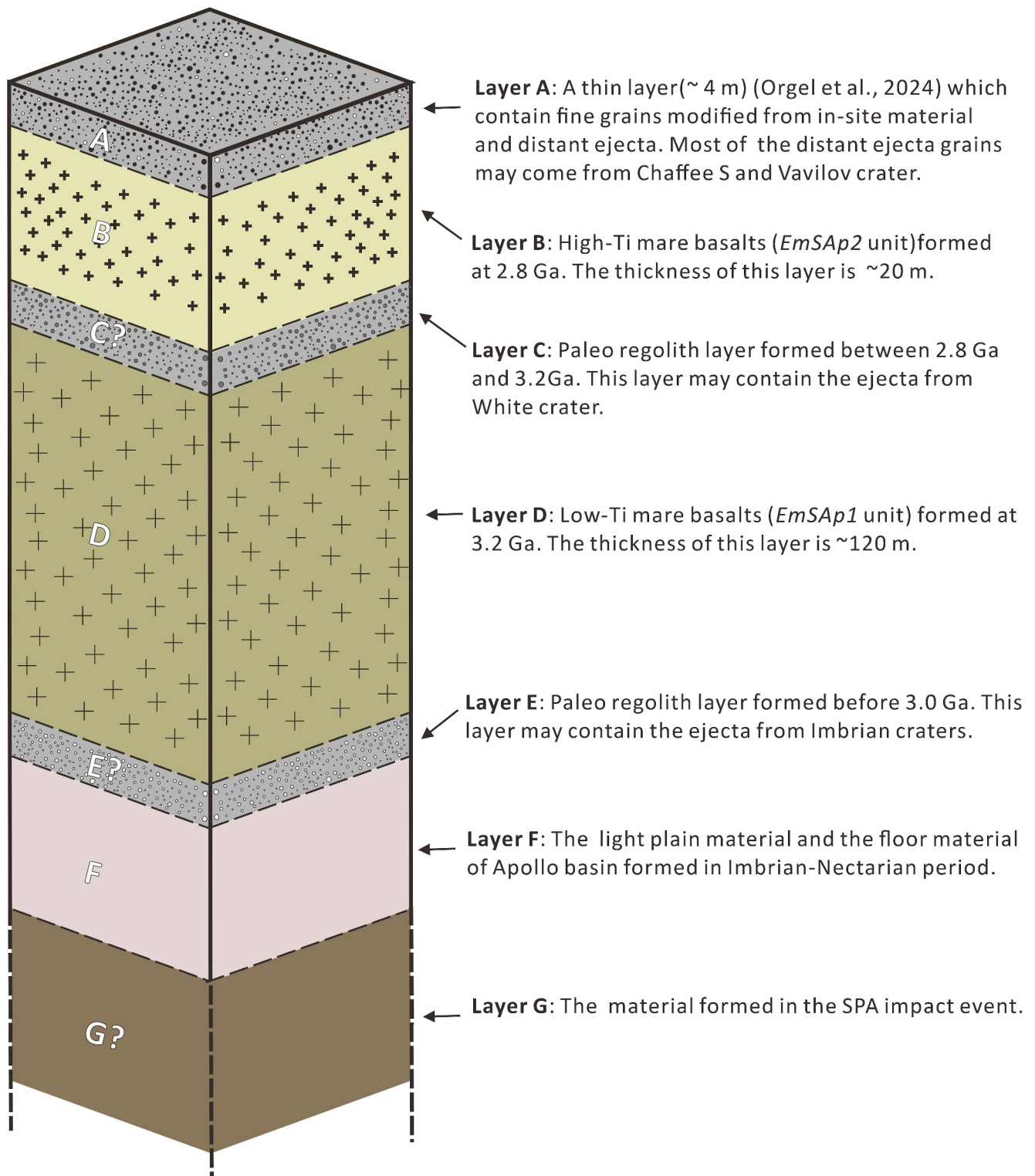### 5.2.4. Copernican Craters Outside of the SPA Basin Rim

Our study suggests that young Copernican craters such as Das, Jackson, Crookes, Vavilov, Guthnik, and Sharonov (Fortezzo et al., 2020; Ivanov et al., 2018; Ravi et al., 2016) might contribute approximately 11.5 cm of ejecta in total to the CE-6 landing area considering the craters beyond the SPA basin rim (Table 4). These materials originate from the FHT outside the SPA basin (Figure S2 in Supporting Information S1).

It is important to note that the thickness of the ejected material calculated here from remote impacts represents the maximum thickness under ideal conditions. In reality, the distribution of the ejected material is not continuous, and at specific points, the actual amount of sputtered material that lands may be minimal or even absent. Generally, the proportion of Copernican crater ejecta outside the SPA basin in the top 95 cm regolith would be 12.1%. The total feldspathic exotic components make up 30.2%, with Chaffee S and Vavilov craters being the major sources. According to the mineral composition measured by Li et al. (2024), the total abundance of Al_2O_3 in CE-6 regolith sample is 14.3–14.4 wt.%, while the abundance of Al_2O_3 in the subophitic basalt is 9.85 wt.%. This difference may be caused by the addition of more than 30% feldspathic material. Therefore, the sample characteristics measured by Li et al. (2024) can be consistent with the proportion in our study.

5.3. Geologic History

Based on the geological mapping and CSFD results from this study, we have further refined the geological evolution of the CE-6 landing site and summarized it in a stratigraphic column (Figure 11).

Before 3.98 Ga, this area was covered by the material formed during the SPA impact event (Layer G in Figure 11). Then at ~3.98 Ga, the Apollo impact event created the layer of Apollo Basin Floor material. Between 3.98 Ga and 3.2 Ga, the CE-6 landing site was covered by highly degraded *Imbrian-Nectarian Apollo Basin Floor* (*INabf* unit) or light plain (*Ip*) material (Layer F in Figure 10). Ejecta from Imbrian impact craters formed a paleolunar regolith layer (Layer E). Around 3.2 Ga, one or multiple episodes of low-Ti basalt flows covered the CE-6 landing site, forming the *EmSAp1* mare unit, with a thickness of 100–120 m (Layer D). Before 2.8 Ga, the White crater excavated mafic materials and transported them to the landing site. The mixing of in situ basaltic materials and Eratosthenian crater ejecta formed another paleoregolith layer (Layer C). Around 2.8 Ga, smaller-scale high-ti basalt activity began from the center of the mare plain and extended outward, forming the *EmSAp2* unit. At the landing site, a thin layer of high-ti basalt, approximately 20 m thick, covered the area (Layer B). Subsequently, the Chaffee S crater and younger Copernican craters further mixed materials from different layers in situ with distant ejecta, forming a compositionally diverse lunar regolith layer at the CE-6 landing site (Layer A). Orgel et al. (2024) measured the thickness of the regolith in the *EmSAp2* unit with an average value of 4.6 m. The thickness of Layer A might be similar to this value.

Layer A: A thin layer(~ 4 m) (Orgel et al., 2024) which contain fine grains modified from in-site material and distant ejecta. Most of the distant ejecta grains may come from Chaffee S and Vavilov crater.

Layer B: High-Ti mare basalts (*EmSAp2* unit)formed at 2.8 Ga. The thickness of this layer is ~20 m.

Layer C: Paleo regolith layer formed between 2.8 Ga and 3.2Ga. This layer may contain the ejecta from White crater.

Layer D: Low-Ti mare basalts (*EmSAp1* unit) formed at 3.2 Ga. The thickness of this layer is ~120 m.

Layer E: Paleo regolith layer formed before 3.0 Ga. This layer may contain the ejecta from Imbrian craters.

Layer F: The light plain material and the floor material of Apollo basin formed in Imbrian-Nectarian period.

Layer G: The material formed in the SPA impact event.

Figure 11. Geological column of the region surrounding the CE-6 landing site.

5.4. Potential Science Value

Using the reconstruction of the geological history above, we can now evaluate the potential areas of scientific value in the returned samples.

The CE-6 site is located in the northeastern part of the *EmSAp2* basalt unit. According to our CSFD results, the *EmSAp2* unit (2.81 Ga) may be one of the youngest basalt units located within the SPA terrane on the far side. A detailed comparative analysis between the young mare basalt unit of lunar nearside and farside may provide clues for further understanding the formation and evolution of lunar basalts and the cause of the lunar nearside-far side dichotomy. Additionally, the crystallization age of another young basalt unit would help refine the lunar CF.

Furthermore, the landing site is near the boundary between the *EmSAp3, EmSAp2* and *EmSAp1*-E units. Impact events may transport younger high-ti basalt and older low-ti basalt to the CE-6 landing site. Additionally, several impact craters with identifiable low-Ti ejecta blankets around the site appear to have excavated the underlying low-Ti basalt to the surface. Therefore, the samples collected from this area may contain basalt from three volcanic periods, spanning up to one billion years.

Ejecta from distant impact craters also enhance the diversity of the regolith samples collected by CE-6. Recent research reveals intriguing compositional characteristics in the ejecta from the Chaffee S and White craters (Jia et al., 2024). The Chaffee S crater ejecta has the highest plagioclase content in the region and may represent materials different from the typical surface of the Apollo basin. Jia et al. (2024) suggested that Chaffee S may have ejected Mg-rich materials to the mare plain around the CE-6 landing site, which could be the lunar crust altered by magnesian magma (Jia et al., 2024). This material could also be the impact melt from the Apollo basin. In this case, Chaffee S crater ejecta in the CE-6 sample could provide clues to determine the isotopic age of the Apollo basin (Yue et al., 2024) and help researchers gain a more comprehensive understanding of the lunar early impact history.

The distant craters may have also transported materials from different compositional terrains in the SPA basin to the landing site. According to the division suggested by Moriarty and Pieters (2016), the CE-6 landing site is located in the OPX Annulus (OPX-A) mineral belt, with the R1 and O'Day craters in the Heterogeneous Annulus (HET-A) mineral belt and the W2 crater in the central SPA Compositional Anomaly (SPACA) mineral belt. Notably, the W2 crater is located on the "Mons White" topographic uplift, named by Jia et al. (2024), which has multiple possible origins (Jia et al., 2024). Thus, W2,R1 and O'Day crater materials in the CE-6 sample can potentially provide compositional information about the different mineral belts within the SPA terrane. Additionally, young impact craters such as Das, Vavilov, Crookes, Jackson, Guthnik and Sharonov could transport materials from the FHT to the CE-6 landing site. The ejecta, if sampled, can deepen our understanding of the composition and geological characteristics of the lunar farside.

6. Conclusion

In this study, we conducted detailed geological mapping of the landing zone of the CE-6 mission, refined CSFD results based on high-resolution data, and assessed the potential scientific outcomes of the CE-6 returned samples. The main results are as follows.

1. There are 16 different geological units in the CE-6 landing site region, including non-mare units (*pNORA, INabf, Ip, Imc*) impact craters and two mare units (*EmSAp1, EmSAp2 and EmSAp3*), reflecting a 3.9 billion-year complex geological history in the region. CE-6 landed on the surface of *EmSAp2*, which has an AMA of ~2.8 Ga. The major source of the CE-6 regolith sample is likely the local *EmSAp2* basalt. Additionally, as the landing site is close to the boundary between the three basalt units. It is also likely that *EmSAp1* and *EmSAp3* material will be found in the CE-6 regolith sample.
2. High-resolution CSFD measurements suggest that there were multiple periods of volcanic activity in the southern part of the Apollo basin. The first stage (3.19 Ga) formed the *EmSAp1* low-Ti basalt, the second stage (2.8 Ga) formed the *EmSAp2* high-Ti basalt and the later stage (1.94 Ga) formed the *EmSAp3* high-Ti basalt. Thus, volcanic activity occurred for longer in this region than previously thought. The returned regolith may thus contain basalt from three volcanic periods, spanning up to one billion years.
3. Impact craters such as Chaffee S, W2, R1, O'Day, Das, Vavilov, Crookes, Jackson, Guthnik, and Sharonov may have contributed ~30% of feldspathic material to the regolith at the CE-6 landing site. These materials would provide valuable information about the composition and cratering history of the lunar farside.

Data Availability Statement

The LRO WAC mosaic and NAC data are available from the LROC website (http://lroc.sese.asu.edu/). The Kaguya Terrain Camera (TC) data and Multiband Imager (MI) data are available from the SELENE Data Archive (https://darts.isas.jaxa.jp/planet/pdap/selene/index.html.en). The mineral maps (plagioclase, orthopyroxene, clinopyroxene, olivine) and derived optical maturity (OMAT) mosaics are available from USGS Astropedia (https://astrogeology.usgs.gov/search?pmi-target=moon). The crater counting files (scc) of this study are available from the Zenodo repository (Gao, 2024).

References

Baker, D. M. H., Head, J. W., Fassett, C. I., Kadish, S. J., Smith, D. E., Zuber, M. T., & Neumann, G. A. (2011). The transition from complex crater to peak-ring basin on the Moon: New observations from the Lunar Orbiter Laser Altimeter (LOLA) instrument. *Icarus*, *214*(2), 377–393. https://doi.org/10.1016/j.icarus.2011.05.030

Barker, M. K., Mazarico, E., Neumann, G. A., Zuber, M. T., Haruyama, J., & Smith, D. E. (2016). A new lunar digital elevation model from the lunar orbiter laser altimeter and SELENE terrain camera. *Icarus*, *273*, 346–355. https://doi.org/10.1016/j.icarus.2015.07.039

Chen, J., Ling, Z., Liu, J., Chen, S., Ding, X., Chen, J., et al. (2022). Digital and global lithologic mapping of the Moon at a 1:2,500,000 scale. *Science Bulletin*, *67*(20), 2050–2054. https://doi.org/10.1016/j.scib.2022.09.015

Costello, E. S., Ghent, R. R., & Lucey, P. G. (2018). The mixing of lunar regolith: Vital updates to a canonical model. *Icarus*, *314*, 327–344. https://doi.org/10.1016/j.icarus.2018.05.023

Eliason, E. M., McEwen, A. S., Robinson, M. S., Lee, E. S., Becker, T., Gaddis, L. R., et al. (1999). Digital processing for a global multispectral map of the Moon from the clementine UVVIS imaging instrument. In *Paper presented at 30th lunar and planetary science conference*. Lunar and Planetary Institute.

Fagan, A. L., & Neal, C. R. (2016). A new lunar high-Ti basalt type defined from clasts in Apollo 16 breccia 60639. *Geochimica et Cosmochimica Acta*, *173*, 352–372. https://doi.org/10.1016/j.gca.2015.08.007

Federal Geographic Data Committee. (2006). *FGDC Digital Cartographic Standard for Geologic Map Symbolization Section 25-Planetary geology features* (Doc. No. FGDC-STD-013-2006). Retrieved from https://pubs.usgs.gov/tm/2006/11A02/FGDCgeostdTM11A2web_Sec25.pdf

Fortezzo, C. M., & Hare, T. M. (2013). Completed digital renovation of the 1:5,000,000 lunar geologic map series. In *Paper presented at the 44th annual lunar and planetary science conference*. The Woodlands.

Fortezzo, C. M., Spudis, P. D., & Harrel, S. L. (2020). Release of the digital unified global geologic map of the Moon at 1:5,000,000-scale. In *Paper presented at the 51st annual lunar and planetary science conference*. The Woodlands.

Gao, A. (2024). Crater couting files at the CE6 landing site [Dataset]. *Zenodo*. https://doi.org/10.5281/zenodo.13997332

Garrick-Bethell, I., & Zuber, M. T. (2009). Elliptical structure of the lunar South Pole-Aitken basin. *Icarus*, *204*(2), 399–408. https://doi.org/10.1016/j.icarus.2009.05.032

Golombek, M. P., & McGill, G. E. (1983). Grabens, basin tectonics, and the maximum total expansion of the Moon. *Journal of Geophysical Research*, *88*(B4), 3563–3578. https://doi.org/10.1029/JB088iB04p03563

Grier, J. A., McEwen, A. S., Lucey, P. G., Milazzo, M., & Strom, R. G. (2001). Optical maturity of ejecta from large rayed lunar craters. *Journal of Geophysical Research*, *106*(E12), 32847–32862. https://doi.org/10.1029/1999JE001160

Haruyama, J., Ohtake, M., Matsunaga, T., Morota, T., Honda, C., Yokota, Y., et al. (2009). Long-lived volcanism on the lunar farside revealed by SELENE terrain camera. *Science*, *323*(5916), 905–908. https://doi.org/10.1126/science.1163382

Haruyama, J., Ohtake, M., Matsunaga, T., Morota, T., Yokota, Y., Honda, C., et al. (2008). Planned radiometrically calibrated and geometrically corrected products of lunar high-resolution Terrain Camera on SELENE. *Advances in Space Research*, *42*(2), 310–316. https://doi.org/10.1016/j.asr.2007.04.062

Haruyama, J., Ohtake, M., Matsunaga, T., Otake, H., Ishihara, Y., Masuda, K., et al. (2014). Data products of SELENE (Kaguya) terrain camera for future lunar missions. In *Paper presented at the 45th annual lunar and planetary science conference*. The Woodlands.

Head, J. W. (1975). Processes of lunar crater degradation: Changes in style with geologic time. *The Moon*, *12*(3), 299–329. https://doi.org/10.1007/BF02629699

Hiesinger, H., & Head, J. W., III. (2004). Lunar South Pole-aitken impact basin: Topography and mineralogy. In *Paper presented at the 35th lunar and planetary science conference*.

Hiesinger, H., Head, J. W. III, Wolf, U., Jaumann, R., Neukum, G., Ambrose, W. A., & Williams, D. A. (2011). Ages and stratigraphy of lunar mare basalts: A synthesis. In *Recent advances and current research issues in lunar stratigraphy* (Vol. 477, p. 0). Geological Society of America. https://doi.org/10.1130/2011.2477(01)

Hiesinger, H., van der Bogert, C. H., Michael, G., Schmedemann, N., Iqbal, W., Robbins, S. J., et al. (2023). The lunar cratering chronology. *Reviews in Mineralogy and Geochemistry*, *89*(1), 401–451. https://doi.org/10.2138/rmg.2023.89.10

Hiesinger, H., van der Bogert, C. H., Pasckert, J. H., Funcke, L., Giacomini, L., Ostrach, L. R., & Robinson, M. S. (2012). How old are young lunar craters? *Journal of Geophysical Research*, *117*(E12), E00H10. https://doi.org/10.1029/2011JE003935

Housen, K. R., Schmidt, R. M., & Holsapple, K. A. (1983). Crater ejecta scaling laws: Fundamental forms based on dimensional analysis. *Journal of Geophysical Research*, *88*(B3), 2485–2499. https://doi.org/10.1029/JB088iB03p02485

Ivanov, M. A., Hiesinger, H., van der Bogert, C. H., Orgel, C., Pasckert, J. H., & Head, J. W. (2018). Geologic history of the northern portion of the South Pole-Aitken basin on the Moon. *Journal of Geophysical Research: Planets*, *123*(10), 2585–2612. https://doi.org/10.1029/2018JE005590

Jia, Z., Chen, J., Kong, J., Qiao, L., Fu, X., & Ling, Z. (2024). Geologic context of Chang'e-6 candidate landing regions and potential non-mare materials in the returned samples. *Icarus*, *416*, 116107. https://doi.org/10.1016/j.icarus.2024.116107

Jolliff, B., Petro, N., Moriarty, D., Ryan Watkins, P., Head, J. III, & Potter, R. (2021). Sample return from the Moon's South Pole-Aitken Basin. *Bulletin of the American Astronomical Society*, *53*(4), 290. https://doi.org/10.3847/25c2cfeb.5309cd69

Jolliff, B. L., Gillis, J. J., Haskin, L. A., Korotev, R. L., & Wieczorek, M. A. (2000). Major lunar crustal terranes: Surface expressions and crust-mantle origins. *Journal of Geophysical Research*, *105*(E2), 4197–4216. https://doi.org/10.1029/1999JE001103

Kneissl, T., van Gasselt, S., & Neukum, G. (2011). Map-projection-independent crater size-frequency determination in GIS environments—New software tool for ArcGIS. *Planetary and Space Science*, *59*(11), 1243–1254. https://doi.org/10.1016/j.pss.2010.03.015

Lemelin, M., Lucey, P. G., Gaddis, L. R., Hare, T. M., & Ohtake, M. (2016). Global map products from the Kaguya Multiband imager at 512 ppd: Minerals, FeO, and OMAT. In *Paper presented at the 47th annual lunar and planetary science conference*. The Woodlands.

Lemelin, M., Lucey, P. G., Miljković, K., Gaddis, L. R., Hare, T., & Ohtake, M. (2019). The compositions of the lunar crust and upper mantle: Spectral analysis of the inner rings of lunar impact basins. *Planetary and Space Science*, *165*, 230–243. https://doi.org/10.1016/j.pss.2018.10.003

Lemelin, M., Lucey, P. G., Song, E., & Taylor, G. J. (2015). Lunar central peak mineralogy and iron content using the Kaguya Multiband Imager: Reassessment of the compositional structure of the lunar crust. *Journal of Geophysical Research: Planets*, *120*(5), 869–887. https://doi.org/10.1002/2014JE004778

Li, C., Hu, H., Yang, M.-F., Liu, J., Zhou, Q., Ren, X., et al. (2024). Nature of the lunar farside samples returned by the Chang'E-6 mission. *National Science Review*, *11*(11), nwae328. https://doi.org/10.1093/nsr/nwae328

Liu, Z., Peng, M., Di, K., Wan, W., Liu, B., Wang, Y., et al. (2024). High-precision visual localization of the Chang'e-6 lander. *National Remote Sensing Bulletin*, *28*(6), 1649–1656. https://doi.org/10.11834/jrs.20244229

Lucey, P. G., Blewett, D. T., Taylor, G. J., & Hawke, B. R. (2000). Imaging of lunar surface maturity. *Journal of Geophysical Research*, *105*(E8), 20377–20386. https://doi.org/10.1029/1999JE001110

Ma, M., Chen, J., Chen, S., Chao, S., Lu, T., Han, C., & Tian, P. (2023). A new method for the identification of lunar cryptomaria and their analysis in the schiller-schickard region. *Journal of Geophysical Research: Planets*, *128*(6), e2022JE007491. https://doi.org/10.1029/2022JE007491

McEwen, A. S., & Bierhaus, E. B. (2006). The importance of secondary cratering to age constraints on planetary surfaces. *Annual Review of Earth and Planetary Sciences*, *34*(1), 535–567. https://doi.org/10.1146/annurev.earth.34.031405.125018

Melosh, H. J. (1989). Impact cratering: A geologic process.

Melosh, H. J., Kendall, J., Horgan, B., Johnson, B. C., Bowling, T., Lucey, P. G., & Taylor, G. J. (2017). South Pole–Aitken basin ejecta reveal the Moon's upper mantle. *Geology*, *45*(12), 1063–1066. https://doi.org/10.1130/G39375.1

Meng, Z., Wang, Y., Chen, S., Zheng, Y., Shi, J., Wang, T., et al. (2019). MTE features of Apollo Basin and its significance in understanding the SPA basin. *Ieee Journal of Selected Topics in Applied Earth Observations and Remote Sensing*, *12*(7), 2575–2583. https://doi.org/10.1109/JSTARS.2019.2916061

Meyer, H. M., Denevi, B. W., Robinson, M. S., & Boyd, A. K. (2020). The global distribution of lunar light plains from the lunar reconnaissance orbiter camera. *Journal of Geophysical Research: Planets*, *125*(1), e2019JE006073. https://doi.org/10.1029/2019JE006073

Meyer, H. M., Robinson, M. S., Denevi, B. W., & Boyd, A. K. (2018). A new global map of light plains from the lunar reconnaissance orbiter camera. In *Paper presented at the 49th annual lunar and planetary science conference*. The Woodlands.

Michael, G. G., & Neukum, G. (2010). Planetary surface dating from crater size–frequency distribution measurements: Partial resurfacing events and statistical age uncertainty. *Earth and Planetary Science Letters*, *294*(3), 223–229. https://doi.org/10.1016/j.epsl.2009.12.041

Michael, G. G., Platz, T., Kneissl, T., & Schmedemann, N. (2012). Planetary surface dating from crater size–frequency distribution measurements: Spatial randomness and clustering. *Icarus*, *218*(1), 169–177. https://doi.org/10.1016/j.icarus.2011.11.033

Moriarty, D., Milla, M., Watkins, R., Domingue, D., Valencia, S., Whitten, J., et al. (2022). A preliminary evaluation of resurfacing scenarios across the South Pole—Aitken Basin interior from a mineralogical assessment of craters. In *Paper presented at the 53rd lunar and planetary science conference*. The Woodlands.

Moriarty, D. P., & Pieters, C. M. (2016). South Pole — Aitken basin as a probe to the lunar interior. In *Paper presented at the 47th annual lunar and planetary science conference*. The Woodlands.

Moriarty, D. P., & Pieters, C. M. (2018). The character of south Pole-Aitken basin: Patterns of surface and subsurface composition. *Journal of Geophysical Research: Planets*, *123*(3), 729–747. https://doi.org/10.1002/2017JE005364

Neukum, G. (1983). *Meteoritenbombardement und datierung planetarer oberflachen*. Habilitation Dissertation for Faculty Membership. Ludwigs-Maximilians-Universiẗ at München.

Neukum, G., Ivanov, B. A., & Hartmann, W. K. (2001). Cratering records in the inner solar system in relation to the lunar reference system. *Space Science Reviews*, *96*(1), 55–86. https://doi.org/10.1023/A:1011989004263

Neumann, G. A., Zuber, M. T., Wieczorek, M. A., Head, J. W., Baker, D. M. H., Solomon, S. C., et al. (2015). Lunar impact basins revealed by gravity recovery and interior laboratory measurements. *Science Advances*, *1*(9), e1500852. https://doi.org/10.1126/sciadv.1500852

Ohtake, M., Haruyama, J., Matsunaga, T., Yokota, Y., Morota, T., Honda, C., & team, L. (2008). Performance and scientific objectives of the SELENE (KAGUYA) Multiband imager. *Earth Planets and Space*, *60*(4), 257–264. https://doi.org/10.1186/BF03352789

Orgel, C., Michael, G., Fassett, C. I., van der Bogert, C. H., Riedel, C., Kneissl, T., & Hiesinger, H. (2018). Ancient bombardment of the inner solar system: Reinvestigation of the "fingerprints" of different impactor populations on the lunar surface. *Journal of Geophysical Research: Planets*, *123*(3), 748–762. https://doi.org/10.1002/2017JE005451

Orgel, C., Torres, I., Besse, S., van der Bogert, C. H., Bahia, R., Prissang, R., et al. (2024). Characterization of high-priority landing sites for robotic exploration missions in the Apollo Basin, Moon. *The Planetary Science Journal*, *5*(2), 29. https://doi.org/10.3847/PSJ/ad1108

Otake, H., Ohtake, M., & Hirata, N. (2012). Lunar iron and titanium abundance algorithms based on SELENE (Kaguya) Multiband imager data. In *Paper presented at the 43rd annual lunar and planetary science conference*. The Woodlands.

Passckert, J. H., Hiesinger, H., & van der Bogert, C. H. (2018). Lunar farside volcanism in and around the South Pole–Aitken basin. *Icarus*, *299*, 538–562. https://doi.org/10.1016/j.icarus.2017.07.023

Pieters, C. M., Head, J. W. III, Gaddis, L., Jolliff, B., & Duke, M. (2001). Rock types of South Pole-Aitken basin and extent of basaltic volcanism. *Journal of Geophysical Research*, *106*(E11), 28001–28022. https://doi.org/10.1029/2000JE001414

Pieters, C. M., Staid, M. I., Fischer, E. M., Tompkins, S., & He, G. (1994). A sharper view of impact craters from clementine data. *Science*, *266*(5192), 1844–1848. https://doi.org/10.1126/science.266.5192.1844

Potter, R. W. K., Collins, G. S., Kiefer, W. S., McGovern, P. J., & Kring, D. A. (2012). Constraining the size of the South Pole-Aitken basin impact. *Icarus*, *220*(2), 730–743. https://doi.org/10.1016/j.icarus.2012.05.032

Potter, R. W. K., Head, J. W., Guo, D., Liu, J., & Xiao, L. (2018). The Apollo peak-ring impact basin: Insights into the structure and evolution of the South Pole–Aitken basin. *Icarus*, *306*, 139–149. https://doi.org/10.1016/j.icarus.2018.02.007

Qian, Y., Head, J., Michalski, J., Wang, X., van der Bogert, C. H., Hiesinger, H., et al. (2024). Long-lasting farside volcanism in the Apollo basin: Chang'e-6 landing site. *Earth and Planetary Science Letters*, *637*, 118737. https://doi.org/10.1016/j.epsl.2024.118737

Qian, Y. Q., Xiao, L., Zhao, S. Y., Zhao, J. N., Huang, J., Flahaut, J., et al. (2018). Geology and scientific significance of the Rümker region in northern oceanus Procellarum: China's Chang'E-5 landing region. *Journal of Geophysical Research: Planets*, *123*(6), 1407–1430. https://doi.org/10.1029/2018JE005595

Qiao, L., Xu, L., Head, J. W., Chen, J., Zhang, Y., Li, B., & Ling, Z. (2024). Geological evidence for extensive basin ejecta as plains terrains in the Moon's South Polar Region. *Nature Communications*, *15*(1), 5783. https://doi.org/10.1038/s41467-024-50155-w

Ravi, S., Meyer, H. M., Mahanti, P., & Robinson, M. S. (2016). On the usefulness of optical maturity for relative age classification of fresh craters. *Paper presented at the AGU Fall Meeting Abstracts.*

Robinson, M. S., Brylow, S. M., Tschimmel, M., Humm, D., Lawrence, S. J., Thomas, P. C., et al. (2010). Lunar reconnaissance orbiter camera (LROC) instrument overview. *Space Science Reviews*, *150*(1), 81–124. https://doi.org/10.1007/s11214-010-9634-2

Sharpton, V. L. (2014). Outcrops on lunar crater rims: Implications for rim construction mechanisms, ejecta volumes and excavation depths. *Journal of Geophysical Research: Planets*, *119*(1), 154–168. https://doi.org/10.1002/2013JE004523

Smith, D. H., Pieters, C. F., & Paulikas, G. A. (2006). The scientific context for the exploration of the Moon. In *Paper presented at the AAS/division for planetary sciences meeting abstracts.*

van der Bogert, C. H., & Hiesinger, H. (2020). Which samples are needed for improved calibration of the lunar cratering chronology? In *Paper presented at the 51st annual lunar and planetary science conference*. The Woodlands.

Wang, X., Head, J. W., Chen, Y., Zhao, F., Kreslavsky, M. A., Wilson, L., et al. (2024a). Lunar farside south Pole-Aitken basin interior: Evidence for more extensive central cryptomaria in the South Pole-Aitken compositional anomaly (SPACA). *Journal of Geophysical Research: Planets*, *129*(5), e2023JE008176. https://doi.org/10.1029/2023JE008176

Wang, Y., Nan, J., Zhao, C., Xie, B., Gou, S., Yue, Z., et al. (2024b). A catalogue of impact craters and surface age analysis in the Chang'e-6 landing area. *Remote Sensing*, *16*(11), 2014. https://doi.org/10.3390/rs16112014

Whitten, J. L., & Head, J. W. (2015). Lunar cryptomaria: Physical characteristics, distribution, and implications for ancient volcanism. *Icarus*, *247*, 150–171. https://doi.org/10.1016/j.icarus.2014.09.031

Wilhelms, D. E., & McCauley, J. F. (1971). Geologic map of the near side of the Moon (703). https://doi.org/10.3133/i703

Wilhelms, D. E., McCauley, J. F., & Trask, N. J. (1987). The geologic history of the Moon (1348). https://doi.org/10.3133/pp1348

Yang, W., He, Y., Qian, Y., & Yue, Z. (2024). Scientists eager for Chang'e-6 lunar farside samples to bring new discoveries. *The Innovation*, *5*(5), 100660. https://doi.org/10.1016/j.xinn.2024.100660

Yue, Z., Di, K., Wan, W., Liu, Z., Gou, S., Liu, B., et al. (2022). Updated lunar cratering chronology model with the radiometric age of Chang'e-5 samples. *Nature Astronomy*, *6*(5), 541–545. https://doi.org/10.1038/s41550-022-01604-3

Yue, Z., Gou, S., Sun, S., Yang, W., Chen, Y., Wang, Y., et al. (2024). Geological context of Chang'e-6 landing area and implications for sample analysis. *The Innovation*, *5*(5), 100663. https://doi.org/10.1016/j.xinn.2024.100663

Zeng, X., Liu, D., Chen, Y., Zhou, Q., Ren, X., Zhang, Z., et al. (2023). Landing site of the Chang'e-6 lunar farside sample return mission from the Apollo basin. *Nature Astronomy*, *7*(10), 1188–1197. https://doi.org/10.1038/s41550-023-02038-1